

Chapter 7. An Example Simulation

The basic concepts presented in Chapter 1 dealt with an ideal RFA network with no dynamics and no transmissive losses. The material in Chapters 2-4 constitutes a more realistic characterization of an RFA network implementation in which these issues are addressed. In the interest of analytical tractability, the physical model for the electrical system was approximated by the Nominal System Model in Chapters 5-6. This model retained some, but by no means all, of the electrical system attributes. With this model, it became easier to discuss structural control system characteristics and design for RFA networks, without getting mired in the details of switching dynamics, nonlinearities of the electrical network, sensory time delay, and so forth. Ultimately, analysis of the Nominal System Model led to the Clipped-Linear feedback controller, several variants of which are discussed in Chapter 6. The behavior of these Clipped-Linear controllers was demonstrated in Chapter 6, for impulsive as well as stationary stochastic disturbances.

It remains to demonstrate the behavior of the complete physical system model; i.e., the assimilation of the nonlinear electrical modeling discussed in Chapters 2-4, the structural dynamics, and the structural control system designs discussed in Chapters 5-6. In this chapter, the physical model of the complete system is simulated, for a structure subjected to earthquake excitation.

7.1: Example System Model

For this example, the two-machine model from Chapters 3-4 will be used. For the structural system, the linear structural model in Fig. 5.5a, used in Example 1 of Chapter 5 and all the examples in Chapter 6, will be used. For convenience, relevant physical quantities for this actuator-structure system are shown in Table 7.1.

The simulated system is illustrated in Fig. 7.1. Many of the characteristics of this system have been discussed in previous chapters. However, there are a few items which should be noted.

- ***Structural sensory data.*** The simulation assumes access to the full, uncorrupted state vector. In actuality, this would probably not be the case. Rather, the sensory data would likely be noise-corrupted acceleration measurements, which would then be used to approximately

Table 7.1: Parameters of the Physical Model

J_1, J_2	$2.27 \times 10^{-4} \text{ Nms}^2$	R_S	500Ω	M	$\begin{bmatrix} 98.3 & 0 & 0 \\ 0 & 98.3 & 0 \\ 0 & 0 & 98.3 \end{bmatrix} \text{ kg}$
B_1, B_2	$1 \times 10^{-4} \text{ Nms}$	C_S	$40 \mu\text{F}$		
η_1, η_2	0.9	R_R	1Ω		
R_1, R_2	0.29Ω	L_R	2 mH	C	$\begin{bmatrix} 175 & -50 & 0 \\ -50 & 100 & -50 \\ 0 & -50 & 50 \end{bmatrix} \text{ Ns/m}$
L_1, L_2	58 mH	V_{sw}	1.4 V		
K_{t1}, K_{t2}	0.37 Nm/A	K_v	2		
l_1	1.33 mm/rad	K	0.5	K	$\begin{bmatrix} 1196 & -684 & 0 \\ -684 & 1370 & -684 \\ 0 & -684 & 684 \end{bmatrix} \text{ kN/m}$
l_2	6.67 mm/rad	C_{c11}	133 kNs/m		
i_{1max}, i_{2max}	3A	C_{c22}	5.31 kNs/m		
f_{1max}	833 N	v_{sw1}	0.504 cm/s	m_{damper}	2.95 kg
f_{2max}	167 N	v_{sw2}	2.52 cm/s	c_{damper}	0.202 Ns/m
				k_{damper}	3.45 kN/m

reconstruct the state vector through a Kalman filter. However, in the interest of simplicity, this practical aspect has been ignored in the present study.

- **Base acceleration sampling.** It is assumed that, in addition to the instantaneous measurement of the structural state, the base acceleration $a_g(t)$ can also be measured instantaneously, and incorporated into the generalized deterministic CL control law, as derived in Eq. (6.73).
- **Digital controller implementation.** The state vector is assumed to be digitally sampled at a frequency of 2 kHz. Following each sample, the force command is computed through the CL control law. It is assumed that the computational time necessary for this is negligible. The computed force command \mathbf{f}_e^* is then issued to the power-electronic control system. To provide a continuous command signal, \mathbf{f}_e^* is sent through an ideal zero-order-hold D/A converter.
- **Force sensing.** The force vector \mathbf{f}_e was assumed to be sensed through current sensing at the terminals of each machine. The effect of the screw conversion efficiency factor \mathbf{H} is not accounted for in the control law (i.e., it is assumed that $\mathbf{H} \approx \mathbf{I}$ when computing \mathbf{f}_e^*) but the 90% efficiencies of each conversion are enforced in the simulation. This effectively introduces a multiplicative parametric uncertainty into the system.
- **Switching controller.** The switching frequency is designed to be around 20 kHz for the \mathbf{f}_e vector. The hysteretic switching controller discussed in Chapter 4 is assumed to be implemented using analog circuitry (with the time-varying hysteresis bands being computed digitally). To determine the switch states D_1 and D_2 , as in Eq. (4.41), V_S is filtered to remove the switching noise on the DC bus. The filter is first-order minimum-phase, with a bandwidth of 250 Hz. For the issuance of the V_S^* command, it is assumed that the switch conduction voltage V_{sw} can be measured precisely. Here, V_{sw} is taken to be constant, at 1.4 V. Although

There are two main issues which govern the bandwidth limitation. The simpler of the two issues concerns the structural sampling frequency. The bandwidth of the controller should be well below this value. The second issue concerns the electrical dynamics of the physical model. Because these dynamics are highly nonlinear, the bandwidth of the electrical response will vary for different operating points and different values of \mathbf{v} . However, some generalizations can be made. Note that, for the electronic design considered here, the time constant τ is equal to 0.02s. As a consequence of this, the bandwidth of the electrical system can be expected to be at least 50Hz at any operating point. For most operating points (and particularly for \mathbf{v} large) the bandwidth will be significantly higher, and it was found that it is unnecessarily conservative to limit the controller bandwidth to 50Hz.

To limit the controller bandwidth, consider a modification of Eq. (7.1) as follows.

$$\begin{aligned}
 J = & \int_0^{t_f} \left\{ 0.5 \left(\frac{d_1(t)}{1mm} \right)^2 + 1.5 \left(\frac{d_2(t)}{1mm} \right)^2 + 2 \left(\frac{d_3(t)}{1mm} \right)^3 \right\} dt \\
 & + \int_0^{t_f} \left\{ \left(\frac{a_1(t)}{1m/s^2} \right)^2 + \left(\frac{a_2(t)}{1m/s^2} \right)^2 + \left(\frac{a_3(t)}{1m/s^2} \right)^2 \right\} dt \\
 & + \int_0^{t_f} R_{filt} \left\{ \left(\frac{f_{e1}(t) - f_{1filt}(t)}{f_{1max}} \right)^2 + \left(\frac{f_{e2}(t) - f_{2filt}(t)}{f_{2max}} \right)^2 \right\} dt
 \end{aligned} \tag{7.2}$$

where f_{1filt} and f_{2filt} are lowpass-filtered versions of f_{e1} and f_{e2} . Here, the filter is taken to be second-order with critical damping. By adjusting R_{filt} , this augmented performance measure can be used to assign a penalty to controllers which produce significant frequency content above the corner frequency of the filter.

To simulate the controller with this augmented performance measure, filtered versions of f_{e1} and f_{e2} must be augmented to the system states. Having done this, differential equation for the Nominal System Model from Chapter 5 becomes

$$\dot{\mathbf{w}}(t) = \mathbf{A}\mathbf{w}(t) + (\mathbf{B}_u + \mathbf{B}_{ufilt})\mathbf{u}(t) \tag{7.3}$$

where the augmented state vector is

$$\mathbf{w} = \begin{bmatrix} \mathbf{M}_{SA}^{1/2} \mathbf{q} \\ \mathbf{u}_{filt} \\ \mathbf{M}_{SA}^{1/2} \dot{\mathbf{q}} \\ \dot{\mathbf{u}}_{filt} \end{bmatrix} \tag{7.4}$$

and the input matrices for the augmented system are defined as

$$\mathbf{B}_u = \begin{bmatrix} \mathbf{0}_{n+m \times m} \\ \mathbf{M}_{SA}^{-1/2} \mathbf{N} \mathbf{C}_c^{1/2} \\ \mathbf{0}_{m \times m} \end{bmatrix}, \quad \mathbf{B}_{u_{filt}} = \begin{bmatrix} \mathbf{0}_{(2n+m) \times m} \\ \mathbf{I} \end{bmatrix} \quad (7.5)$$

The expressions for the force constraints stay the same.

For this augmented system, the analysis in previous chapters follows in essentially the same way. The only necessary modification to the theory is that there is now a distinction between the total input matrix (i.e., $\mathbf{B}_u + \mathbf{B}_{u_{filt}}$) and the matrix used in the regenerative constraint (i.e., \mathbf{B}_u).

For the example presented in this chapter, this augmented system representation and performance measure is used. The corner frequency for the force filter was taken to be 200Hz, and the value of R_{filt} was taken to be 10^3 .

From Eq. (7.2), the quantities \mathbf{Q} , \mathbf{S} , \mathbf{R} , \mathbf{Q}_a , \mathbf{S}_a , and R_a can be found as discussed in previous chapters. For a given CL control law synthesis method, the derivation of the \mathbf{P} matrix follows as discussed in Chapter 6. From this matrix, the appropriate \mathbf{K}_{CL} and \mathbf{K}_{CLa} matrices can then be found from Eqs. (6.68) and (6.69). With these matrices, the CL control law for deterministic forced response in Eq. (6.73) is fully characterized.

It should be noted that technically the Stochastic Clipped-Optimal and Stochastic Damping Reference controllers studied in the previous chapter assumed zero feed-forward gain; i.e., $\mathbf{K}_{CLa} = \mathbf{0}$. This was necessary in order for the stochastic optimization to be well-posed. However, for deterministic response, better performance is attainable with \mathbf{K}_{CLa} assigned as in Eq. (6.69) for these cases. This does not affect the computation of \mathbf{P} or \mathbf{Z} for these controllers.

7.3: Simulation Results

The performance of the system is evaluated for four earthquake records. Specifically, these are the El Centro (May 18, 1940, N-S component measured at Imperial Valley Irrigation District), Hachinohe (May 16, 1968, N-S component measured at Hachinohe City), Kobe (Jan. 17, 1995, N-S component measured at Japanese Meteorological Agency station), and Northridge (Jan. 17, 1994, N-S component measured at Sylmar County Hospital) records. Because the structure represents a scale-model building, each record has been time-scaled by a factor of 5. These records are shown in Fig. 7.2.

Simulations were performed over the time interval from 0 to 5 seconds. Tables 7.2-7.5 show the response data for the simulated physical system. The tables show the performance of each of the controllers, but also other data of interest. The maximum drift and acceleration for

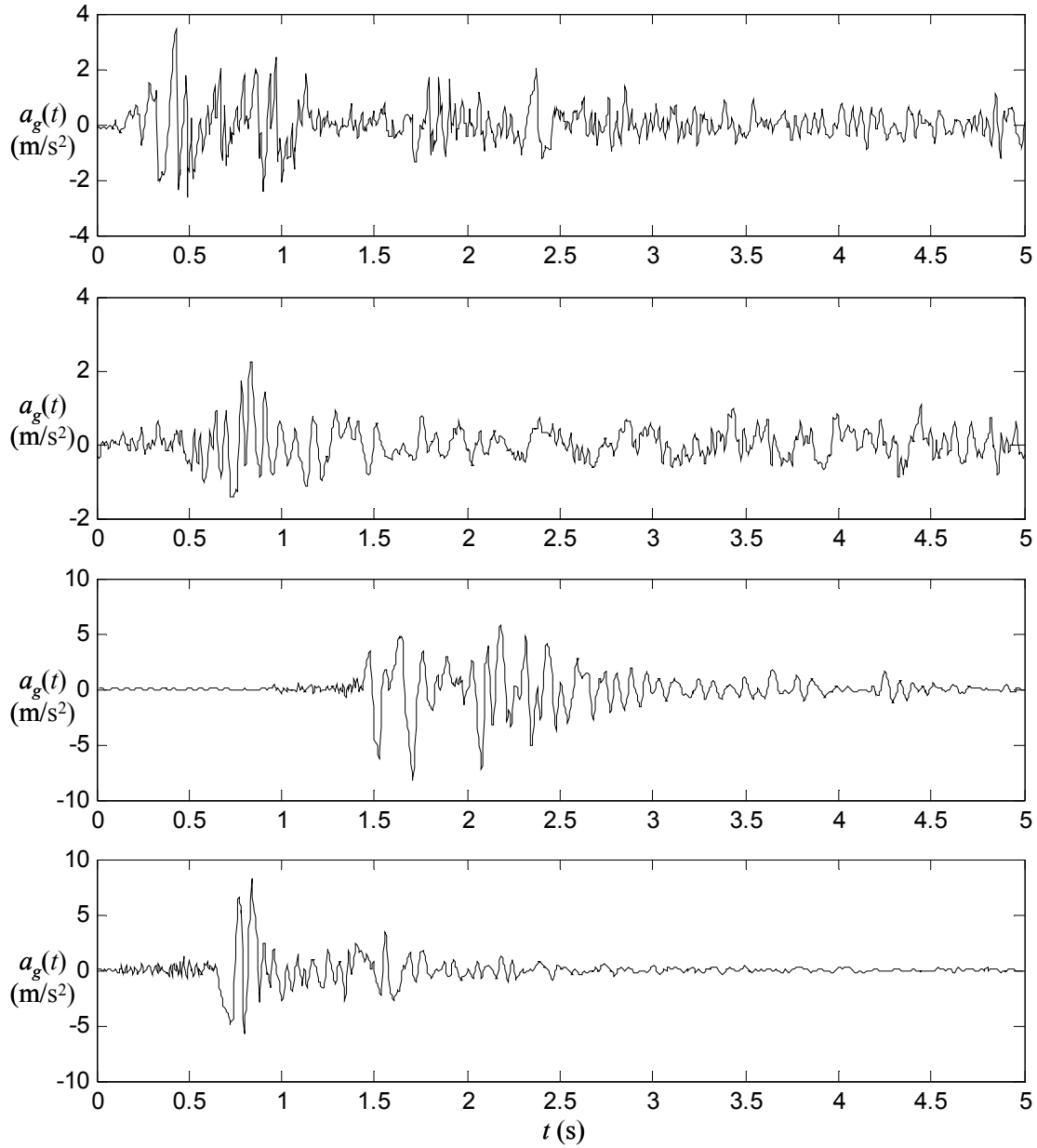


Figure 7.2: El Centro, Hachinohe, Kobe, and Northridge earthquake records (top to bottom)

each degree of freedom and force for each actuator are shown for each controller, as well as for the uncontrolled case. Additionally, data is given for the optimal constant diagonal \mathbf{Z} (DZ) case. Although this case was implemented using the RFA network to provide the forces, the constraint of these forces to a constant damping with diagonal \mathbf{Z} corresponds to an equivalent local viscous damping. As such, this data may be treated as a “baseline” for the judgment of the quality of the controllers, in comparison to traditional viscous damping.

Table 7.2: Response data for the El Centro earthquake record

	CO	DR-S	DR- \mathcal{H}_∞	CZ	DZ	No Control
d_1 (mm)	1.71	1.21	1.19	1.12	1.16	4.57
d_2 (mm)	0.593	0.802	0.880	0.832	0.955	1.93
d_3 (mm)	0.462	0.574	0.608	0.594	0.674	1.11
d_4 (mm)	10.2	10.4	10.4	9.56	1.65	5.79
a_1 (m/s ²)	2.72	2.53	2.34	2.79	3.03	5.73
a_2 (m/s ²)	2.31	2.18	2.25	3.34	3.38	7.09
a_3 (m/s ²)	2.95	3.96	4.13	4.14	4.61	7.61
a_4 (m/s ²)	24.57	13.6	13.7	13.9	3.93	3.19
f_{e1} (N)	474	521	613	462	515	–
f_{e2} (N)	162	82.1	81.8	79.8	13.7	–
J	6.29	6.97	7.39	8.33	9.46	62.43

Table 7.3: Response data for the Hachinohe earthquake record

	CO	DR-S	DR- \mathcal{H}_∞	CZ	DZ	No Control
d_1 (mm)	1.51	1.20	1.20	1.14	1.11	4.97
d_2 (mm)	0.540	0.626	0.622	0.627	0.662	2.19
d_3 (mm)	0.363	0.393	0.384	0.504	0.508	1.31
d_4 (mm)	11.60	9.07	8.84	8.63	1.37	6.51
a_1 (m/s ²)	1.93	2.07	2.06	1.82	1.80	5.35
a_2 (m/s ²)	1.91	2.17	2.22	3.32	3.43	7.38
a_3 (m/s ²)	2.39	2.49	2.37	3.28	3.47	9.01
a_4 (m/s ²)	13.0	11.7	12.3	11.5	2.47	3.51
f_{e1} (N)	441	368	3.59	349	362	–
f_{e2} (N)	67.7	57.6	59.0	54.7	5.33	–
J	5.49	5.24	5.18	5.99	5.66	106

Consider the performances of the various controllers for these four earthquakes. The data yields mixed conclusions concerning which controller is better. The CO controller does best for the El Centro and Kobe earthquakes. For the Northridge earthquake, however, its performance is much worse than both DR controllers. In this case, the DR-S controller out-performs all others, while in the case of the Hachinohe earthquake, the DR- \mathcal{H}_∞ does best.

The data in these tables illustrates the consistency of performance for DR controllers. Note that in all four cases, the DR-S and DR- \mathcal{H}_∞ controllers perform better than the CZ case. However, the CO controller performs worse than even the DZ case for the Northridge earthquake, by a significant margin. Thus, although the disturbances in this example are clearly neither impulsive nor stationary white noise, the observations made in the last chapter concerning the consistency of DR controllers for impulse and stationary stochastic responses appear to carry over fairly well to earthquake responses. The only exception to this occurs for the Hachinohe

Table 7.4: Response data for the Kobe earthquake record

	CO	DR-S	DR- \mathcal{H}_∞	CZ	DZ	No Control
d_1 (mm)	6.42	6.13	6.31	6.26	6.26	12.6
d_2 (mm)	2.05	2.57	2.72	2.79	2.96	5.29
d_3 (mm)	1.30	1.62	1.72	1.68	1.81	3.01
d_4 (mm)	46.3	40.3	40.5	41.8	2.15	25.0
a_1 (m/s ²)	8.80	7.81	7.56	10.2	9.16	14.4
a_2 (m/s ²)	6.55	8.56	8.61	8.71	9.03	19.0
a_3 (m/s ²)	8.78	11.42	12.06	11.8	12.3	20.6
a_4 (m/s ²)	43.2	40.8	40.8	42.6	13.5	12.6
f_{e1} (N)	908	931	896	924	887	–
f_{e2} (N)	177	178	180	178	24.4	–
J	38.8	44.7	48.6	50.6	55.5	1190

Table 7.5: Response data for the Northridge earthquake record

	CO	DR-S	DR- \mathcal{H}_∞	CZ	DZ	No Control
d_1 (mm)	4.34	3.73	4.02	3.13	2.98	6.47
d_2 (mm)	2.73	2.43	2.52	2.36	2.16	3.32
d_3 (mm)	1.74	1.40	1.54	1.40	1.52	2.06
d_4 (mm)	20.5	29.0	29.3	27.0	2.05	24.9
a_1 (m/s ²)	10.7	9.89	10.5	9.32	9.80	9.73
a_2 (m/s ²)	7.60	7.29	7.03	8.03	6.80	10.7
a_3 (m/s ²)	11.6	9.23	10.2	9.91	10.3	14.1
a_4 (m/s ²)	33.4	32.5	33.1	31.7	11.0	12.8
f_{e1} (N)	874	890	896	884	871	–
f_{e2} (N)	174	174	174	169	38.8	–
J	29.4	24.0	25.1	26.5	26.8	187

earthquake, where the DZ case actually out-performs the CZ case. This could not happen for impulsive or stationary responses.

These observations lead to the conclusion that DR controllers, while clearly not out-performing CO controllers in every case, do yield performance which is qualitatively competitive. In addition, they also have a favorable consistency in performance when compared to the CZ case. This observation is significant, because the CZ controller, for the Nominal System Model, yields a linear closed-loop system. Thus, DR controllers can in general be expected to perform favorably in comparison to a system with much more tractable analytical response characteristics.

Consider the rest of the data shown in the tables. Again the conclusions are mixed, concerning the best controller, as few trends exist between the four earthquakes. One of the few notable trends is that DR controllers consistently yield lower first-story drifts, in most cases at the expense of the upper-story drifts. Also, the profile of the drifts in all cases mirrors the weighting

scheme in Eq. (7.2) for the drift quantities, although this observation is also due to the fact that the drifts of the fundamental mode of a shear structure naturally decrease with story number.

The maximum force data is also inconsistent, with various cases yielding different conclusions. For El Centro, f_{e1} is higher for the DR controllers, whereas it is lower for these controllers for Hachinohe. For the Kobe and Northridge earthquakes, which have larger magnitudes, the forces all saturate at their maximum bounds. Note, however, that the maximum force data is larger than f_{1max} and f_{2max} from Table 7.1. This is because of the electronic switching noise present in the forces, which constitutes a high-frequency “ripple” in the stator currents of the machines. However, the force commands, and the average force behavior, do indeed obey the maximum ratings.

To further analyze the response characteristics of the controlled structure, Figs. 7.5-7.20 in the appendix to this chapter show the response data for the four controllers, subjected to the four earthquakes. From this data, there are a number of general conclusions which can be drawn for all the controllers. However, the plots in the appendix represent a fairly large amount of information. To focus the discussion, a few plots pertaining to specific points will be interleaved with the discussion here. However, the qualitative response characteristics discussed here are common to all controllers and all earthquake cases.

First, consider Fig. 7.3, which shows the first second of the response for the DR-S controller, subjected to the El Centro earthquake. There is significant oscillatory power flow for $P_2(t)$, corresponding to the actuator used to excite the tuned mass damper. Following the outset of the earthquake, a significant portion of the energy extracted from the structure near the base is transmitted to the roof. The structure reaches its maximum state of response at approximately $t=0.5s$. At around this time, the mass damper is excited through the power-coupling between the two actuators. This is reflected in the plot of the velocity $v_2(t)$. Compared to the uncontrolled case, $v_2(t)$ undergoes an extremely large response during the first 0.7 seconds. Following this initial period of excitation, the average value of $P_2(t)$ becomes negative, indicating that actuation force $f_{e2}(t)$ is mostly providing damping to the system. This behavior is similar for other controllers, and for other disturbances.

Fig. 7.4 shows the electrical quantities over this same time duration, and for the same controller and earthquake. At the beginning of the disturbance, all the electrical quantities are zero. At approximately 0.17s, the velocity vector \mathbf{v} is large enough to excite currents in the system, causing the network to “come on line,” signified by the DC bus voltage deviating to a nonzero value, and facilitating the power coupling between the devices. However, the velocity

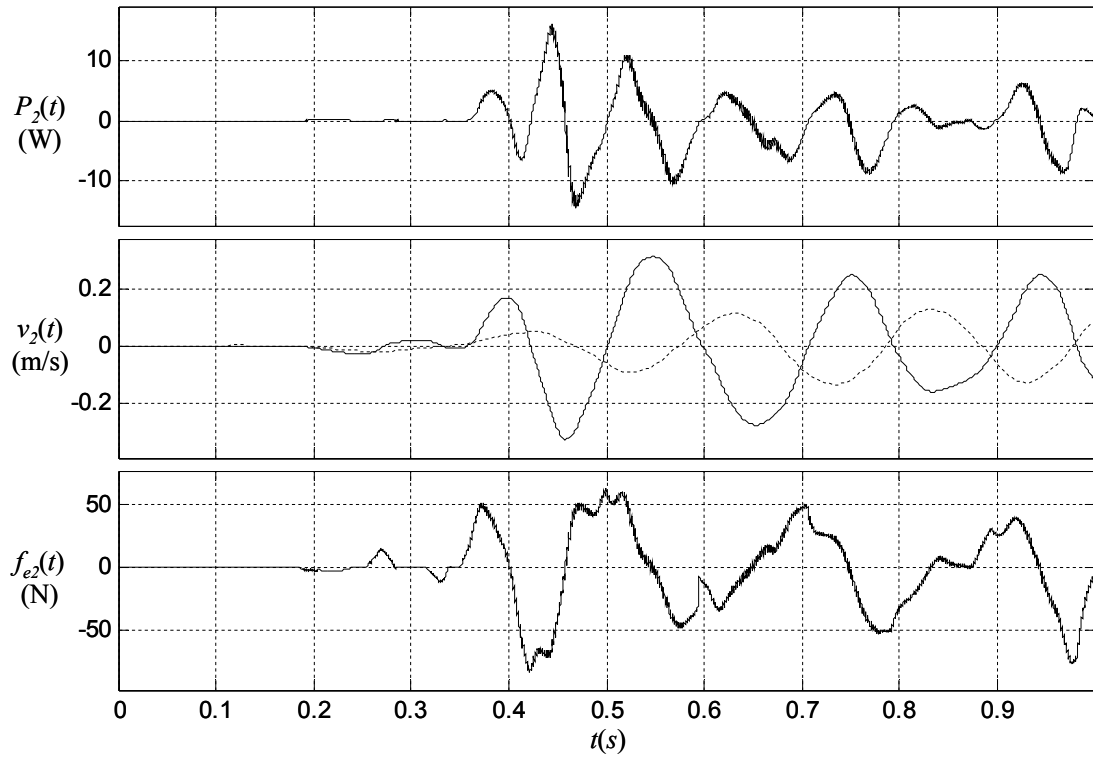


Figure 7.3: Power flow, controlled velocity (solid), uncontrolled velocity (dashed), and electromechanical force for actuator 2 (DR-S controller, El Centro earthquake)

vector is not large enough at this time to produce any sizable force. At approximately 0.35s, the structural response increases dramatically, resulting in extremely large forces for both machines.

Note that, during this period, the electrical quantities noticeably lag their commanded values. This is because the system is operating near the boundary of the feasible force region. In other words, the network is transmitting energy from one actuator to the other with optimum efficiency. As discussed in Chapter 4, uncertainty in the boundary of the feasible region results in a tracking error for the electronic control system in this circumstance. The nonlinear robust controller discussed in Chapter 4 works to reduce this error, but it is still evident in the response. The dissipative interface current $i_R(t)$ may be used as an indicator of times during which the system is operating near the feasible boundary. When $i_R(t)$ is nonzero, this implies that there is excess electrical energy generated, implying operation well inside the feasible region. When $i_R(t)=0$, this implies that the system is operating at maximum efficiency (i.e., on the boundary). Comparing the value of $i_R(t)$ with the force and voltage curves, it is readily apparent that tracking slips only when $i_R(t)=0$. At all other times, the electrical system achieves perfect low-frequency tracking.

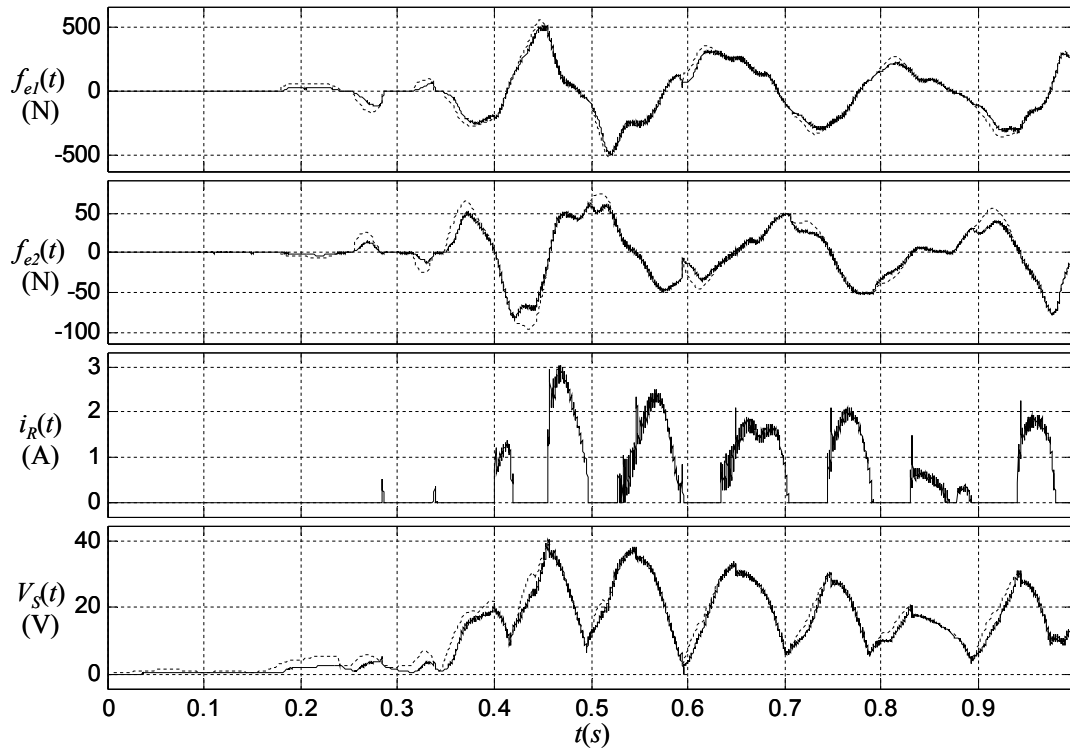


Figure 7.4: Electrical system quantities (solid) and their commands (dashed) (DR-S controller, El Centro earthquake)

To further illustrate this point, consider the responses for $i_R(t)$ for the Kobe earthquake for the CO and DR-S controllers, in Figs. 7.13b and 7.14b, respectively. (Note that plots for the DR- \mathcal{H}_∞ and CZ controllers look very similar to the DR-S case.) It is clear that the CO controller yields operation which is consistently closer to the boundary of the feasible region. This helps to explain why the CO controller yields so much better performance in this case.

As a final thought, consider the first second of the control force response to the Northridge earthquake for the CO and DR-S controllers (in Figs. 7.17a and 7.18a, respectively). The CO controller performed much worse than the others in this circumstance. The data indicates that the CO controller does not issue a significant force command until approximately $t=0.8$ s. By comparison, the DR-S controller produces large forces much earlier on. Because the Northridge earthquake is predominantly impulsive (compared to the El Centro earthquake, for example) this faster reaction clearly influences the performance of the controller.

Scaling Issues

As in previous chapters, the results discussed in this chapter were for a scale model of a prototype structure. It is therefore important to consider, at least briefly, the implications for demands on the control devices which would result from a similar full-scale implementation. From Chapter 5, recall that the scaling between the model and prototype was 1:60 for force, 4:29 for displacement, and 1:5 for time. Consequently, the velocity scaling is approximately 4:6 and power scaling is approximately 1:90.

It therefore follows that the full-scale control implementation corresponding to this study would require force actuators with maximum force ratings of 50kN and 10kN for actuators 1 and 2, respectively. For the examples considered in this chapter, the maximum power requirements are for the Kobe earthquake, and are around 200W for the scale model. Thus, the corresponding power requirement for the prototype structure would be around 18kW.

It must also be considered that the earthquake inputs for these examples were scaled in time, but not in acceleration magnitude. The scaling ratio between model and prototype is 7:2. Consequently, if the controlled prototype structure were subjected to the actual earthquake acceleration records, the force and power requirements would be considerably more than the rescaled quantities found above.

Finally, it is important to note that most commercial control applications involve much larger buildings (and therefore much larger actuator requirements) than the prototype structure on which the scale model was based. This is reflected by the fact that the force requirements for commercial variable-orifice dampers manufactured by Kajima Corporation have forcing capabilities well beyond 1000kN. It may be that the actuator requirements for the prototype structure are not representative of those which would exist for real applications, and that an RFA network with the force and power levels necessary for full-scale operation would require a completely custom design.

Comparison with Semiactive Systems

Speaking qualitatively, comparisons between different nonlinear control devices is difficult because it is not clear what actuator characteristics to normalize between the different device types. (For instance, is it meaningful to compare two devices of equal forcing capability, if their constructions are so radically different that the factors determining maximum force capability are totally different?) Nonetheless, it is interesting to compare the RFA network to a semiactive system to give some insight into the benefit afforded to RFA networks as a consequence of their power-sharing ability.

One useful comparison is to contrast the controlled responses discussed earlier for the RFA network with the analogous cases where the network is not permitted to share power. To do this, consider that the Clipped-Linear structural controller can be redesigned such that it constrains the force commands to the semiactive forcing region. Because \mathbf{R} is diagonal for this example, the clipped-linear semiactive controller can be expressed as

$$f_{ek}^*(t) = c_k(t)v_k(t) \quad (7.6)$$

where $c_k(t)$ is defined as

$$c_k(t) = C_{ckk} \text{sat}_{[-1,0]} \{u_{ak}(t)/v_k(t)\} \quad (7.7)$$

Implemented as such, we are effectively “handicapping” the RFA network, by requiring it to operate only in the forcing region which is also achievable for a semiactive system constructed with the same hardware.

For the response to the Kobe earthquake record, Clipped-Optimal control performed much better than the Damping-Reference methods. Consider Table 7.6, which compares the response data for this earthquake, with Clipped-Optimal control, for the RFA and semiactive cases. Clearly, the RFA network improves considerably upon the response characteristics of the upper two floors. Meanwhile, the response of the bottom floor has maximum quantities which are actually better for the semiactive case. Note that the response of the mass damper for the RFA case is orders of magnitude higher than that of the semiactive case.

It can be concluded that by allowing power to flow directly from the ground to the roof, the RFA network is capable of improving the response of the upper floors of the building. It is interesting that even though the maximum response quantities for these two cases are rather

Table 7.6: Comparison of semiactive and RFA responses for Kobe earthquake record, with Clipped-Optimal control

	semiactive	RFA	% improvement
d_1 (mm)	6.47	6.42	0.789
d_2 (mm)	2.54	2.05	19.1
d_3 (mm)	1.71	1.30	24.3
d_4 (mm)	2.15	46.3	-2050
a_1 (m/s ²)	8.35	8.80	-5.42
a_2 (m/s ²)	8.45	6.55	22.6
a_3 (m/s ²)	11.6	8.78	24.3
a_4 (m/s ²)	14.9	43.2	-189
J	38.7	38.8	-0.230

different, the difference in the performance metric J is rather small. Thus, the control systems are equally effective in minimizing J , but by very different means.

7.4: Conclusions

The physical model of an RFA network is considerably more complicated than the nominal model developed in Chapter 5. As such, one of the two motivations for this chapter was to simulate the response of the physical model of the RFA network in a structural control application. As is shown in the figures in this chapter, the electrical dynamics, switching noise, and uncertainty produce interesting behavior for the combined structure/actuator system.

The second motivation of this chapter was to illustrate the response of RFA networks to earthquake-excited structures. It was shown in examples that the various controllers proposed in the previous chapter perform comparably in this application, with no one controller yielding obviously superior performance. However, the examples also illustrate that the Damping Reference controllers tend to yield responses which are consistently below that of the linear Constant- \mathbf{Z} controller. This observation may be useful control law development for earthquake engineering where, ultimately, the emphasis in control law design is on reliability. In this context, the notion of nonlinear high-performance controllers with guaranteed theoretical performance bounds may be appealing.

Appendix A7: Simulation Plots

Note concerning the plots:

There are two plots for each simulation. These plots have been enumerated *a* and *b*, for convenience. Clockwise from top left, plot *a* shows the drifts for the controlled (solid) and uncontrolled (dashed) cases, absolute accelerations for the controlled (solid) and uncontrolled (dashed) cases, the actuator forces (solid) and their commands (dashed), and the actuator velocities for the controlled (solid) and uncontrolled (dashed) cases.

From top to bottom, plot *b* shows the actuator currents i_1 and i_2 , the dissipative interface current i_R , the DC bus voltage V_S (solid) and its command (dashed), the power flows $P_1=f_{e1}v_1$ and $P_2=f_{e2}v_2$, and the total power flow $P_T=P_1+P_2$.

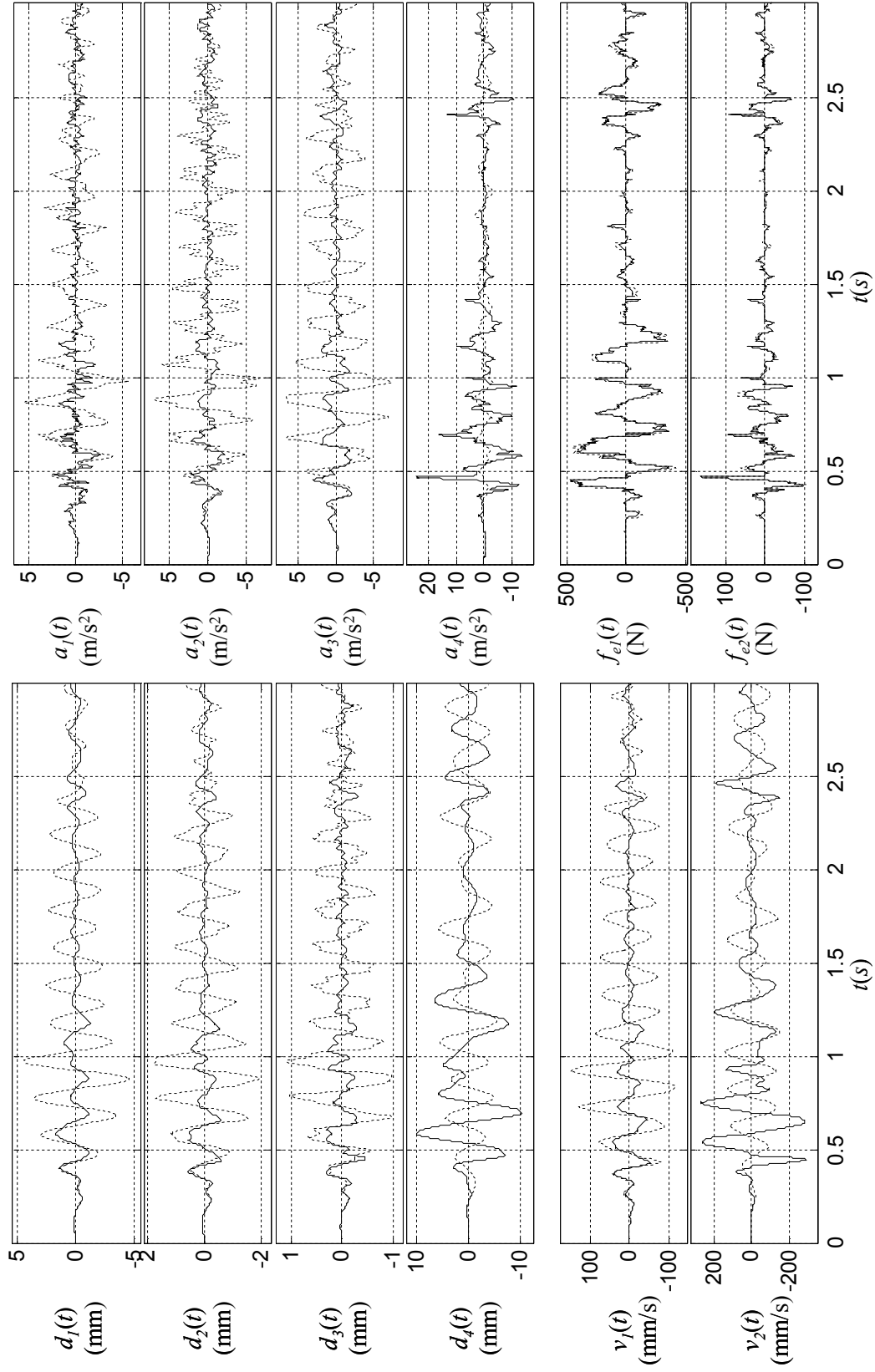


Figure 7.5a: Mechanical response quantities for El Centro earthquake with CO control

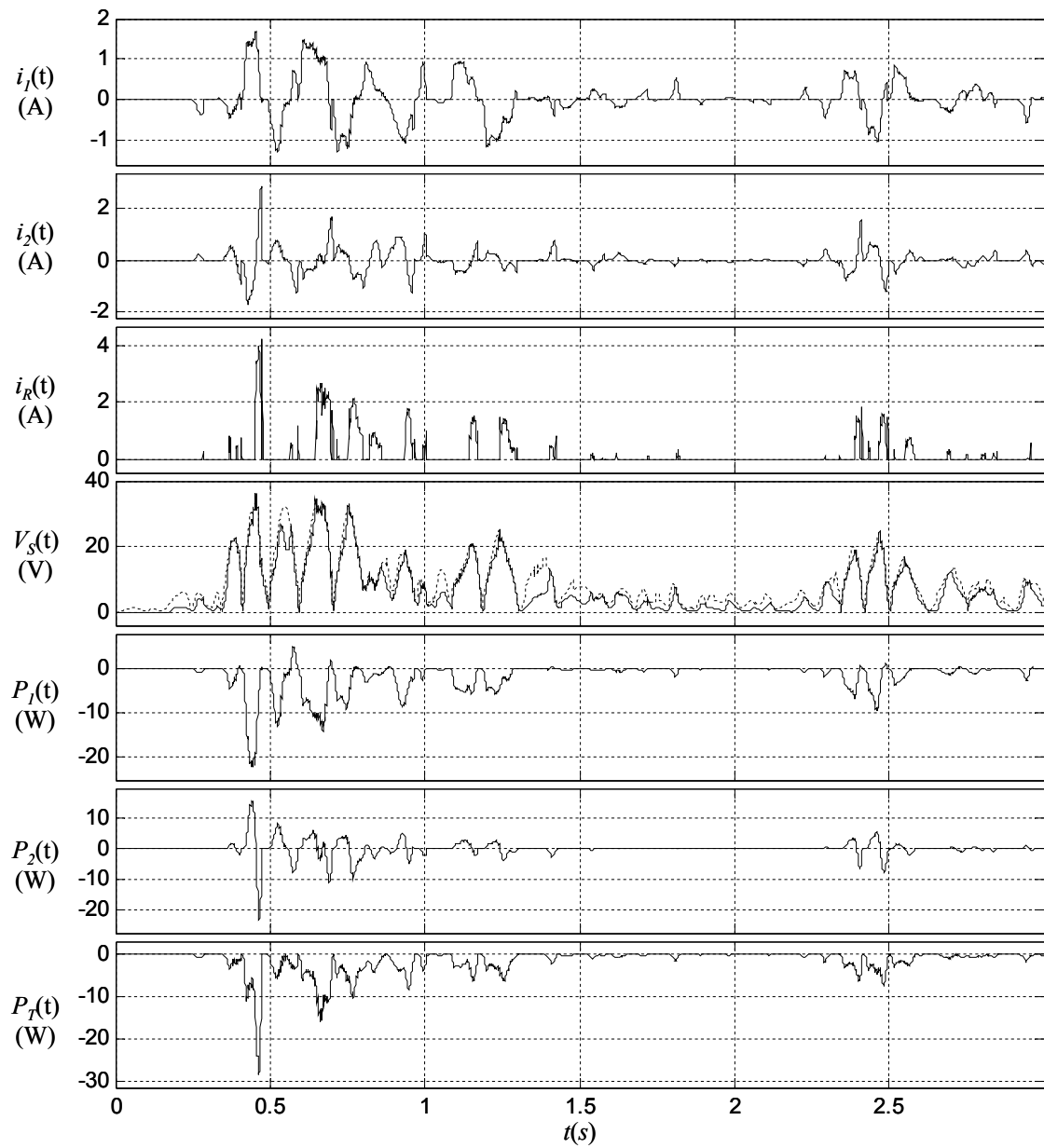


Figure 7.5b: Electrical response quantities for El Centro earthquake with CO control

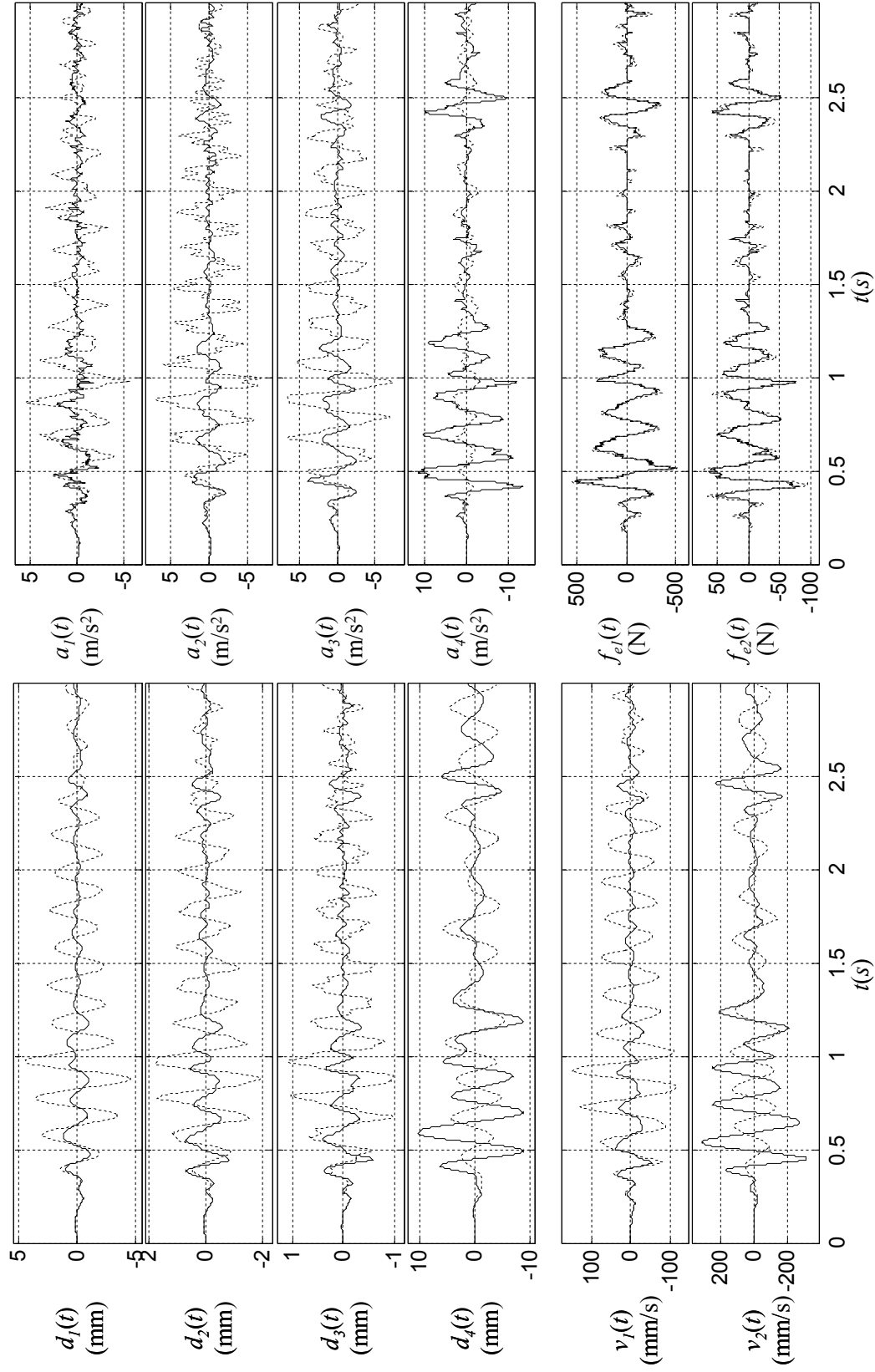


Figure 7.6a: Mechanical response quantities for El Centro earthquake with DR-S control

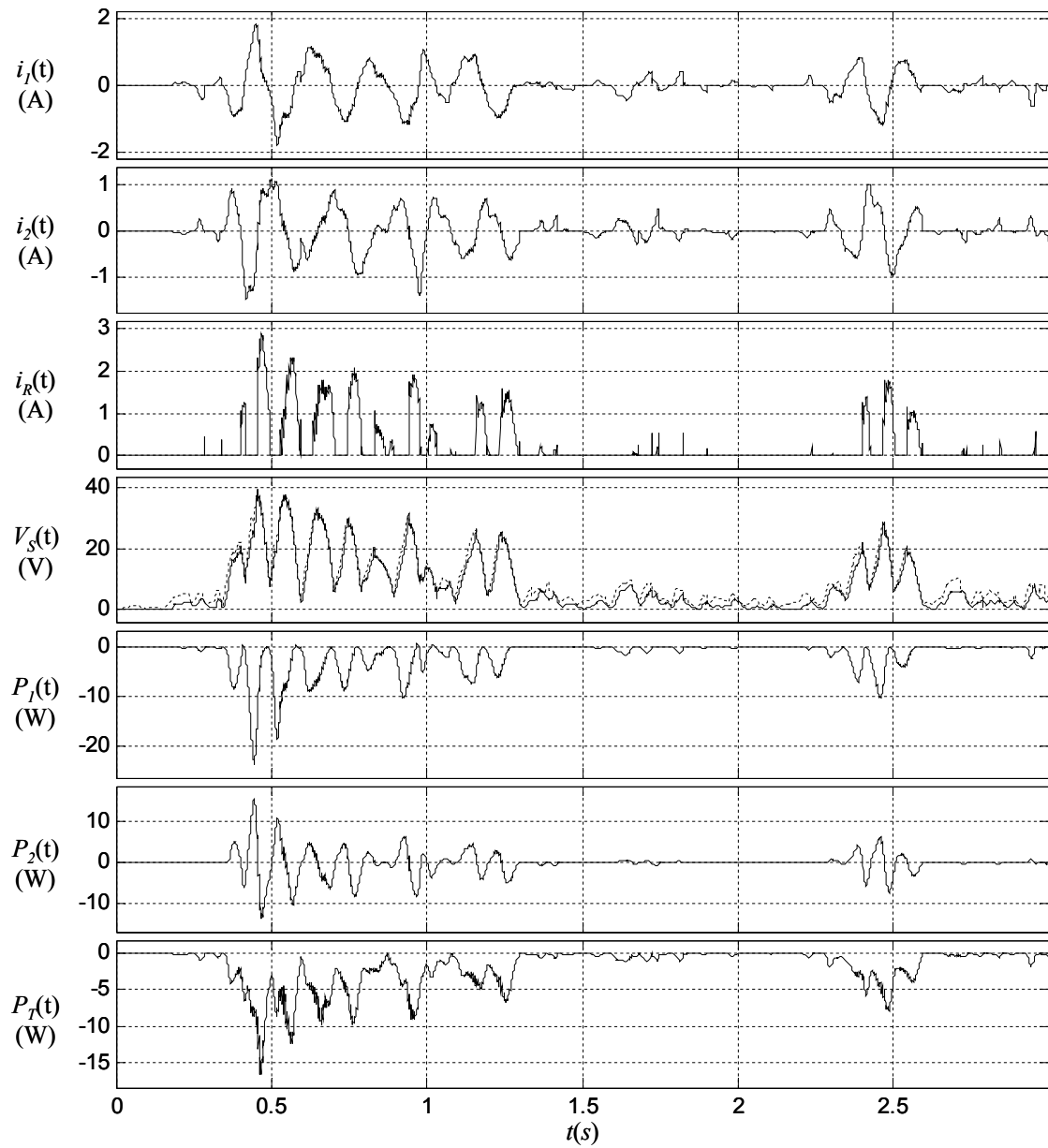
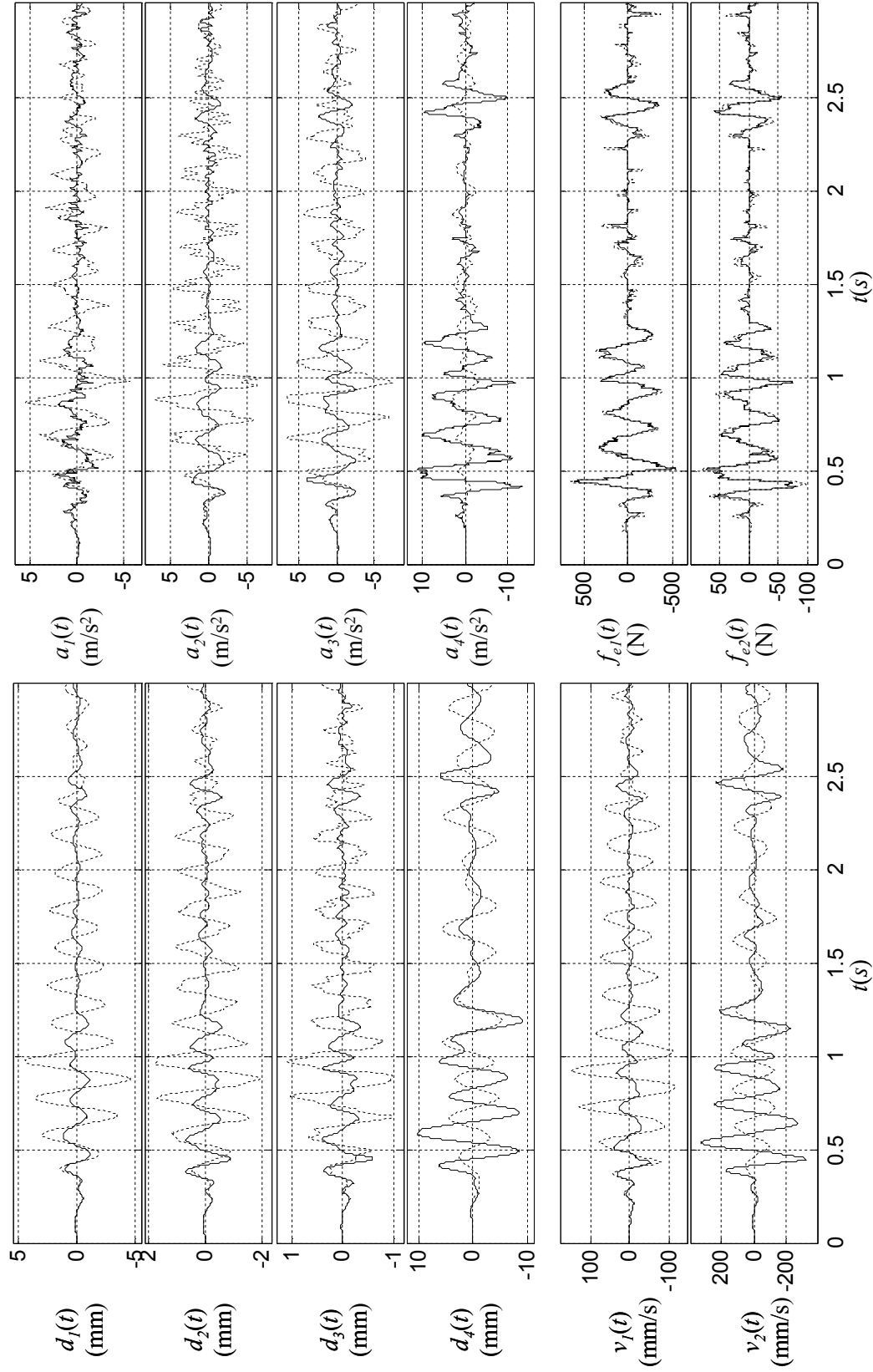


Figure 7.6b: Electrical response quantities for El Centro earthquake with DR-S control

Figure 7.7a: Mechanical response quantities for El Centro earthquake with DR- \mathcal{H}_∞ control

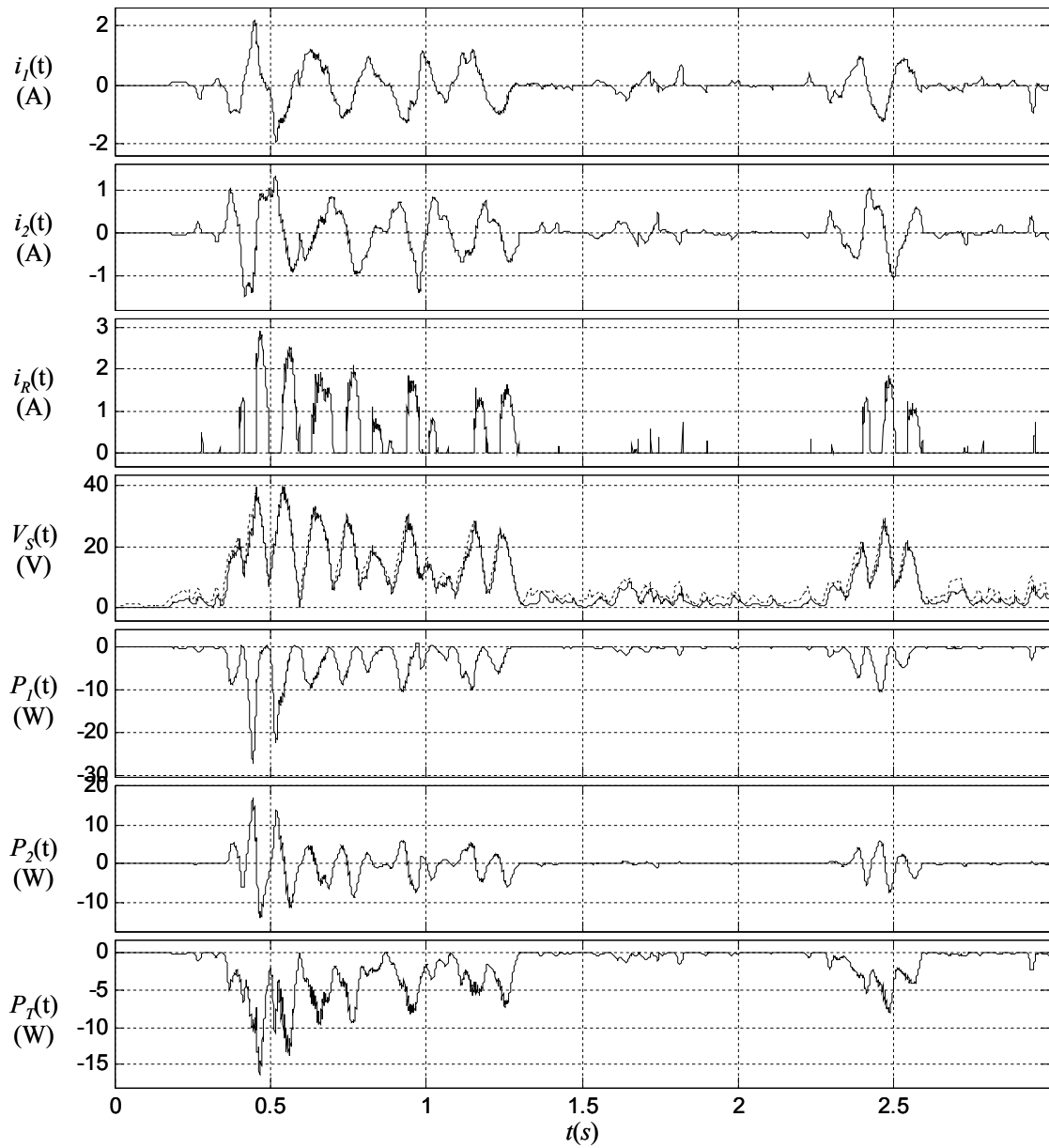


Figure 7.7b: Electrical response quantities for El Centro earthquake with DR- \mathcal{H}_∞ control

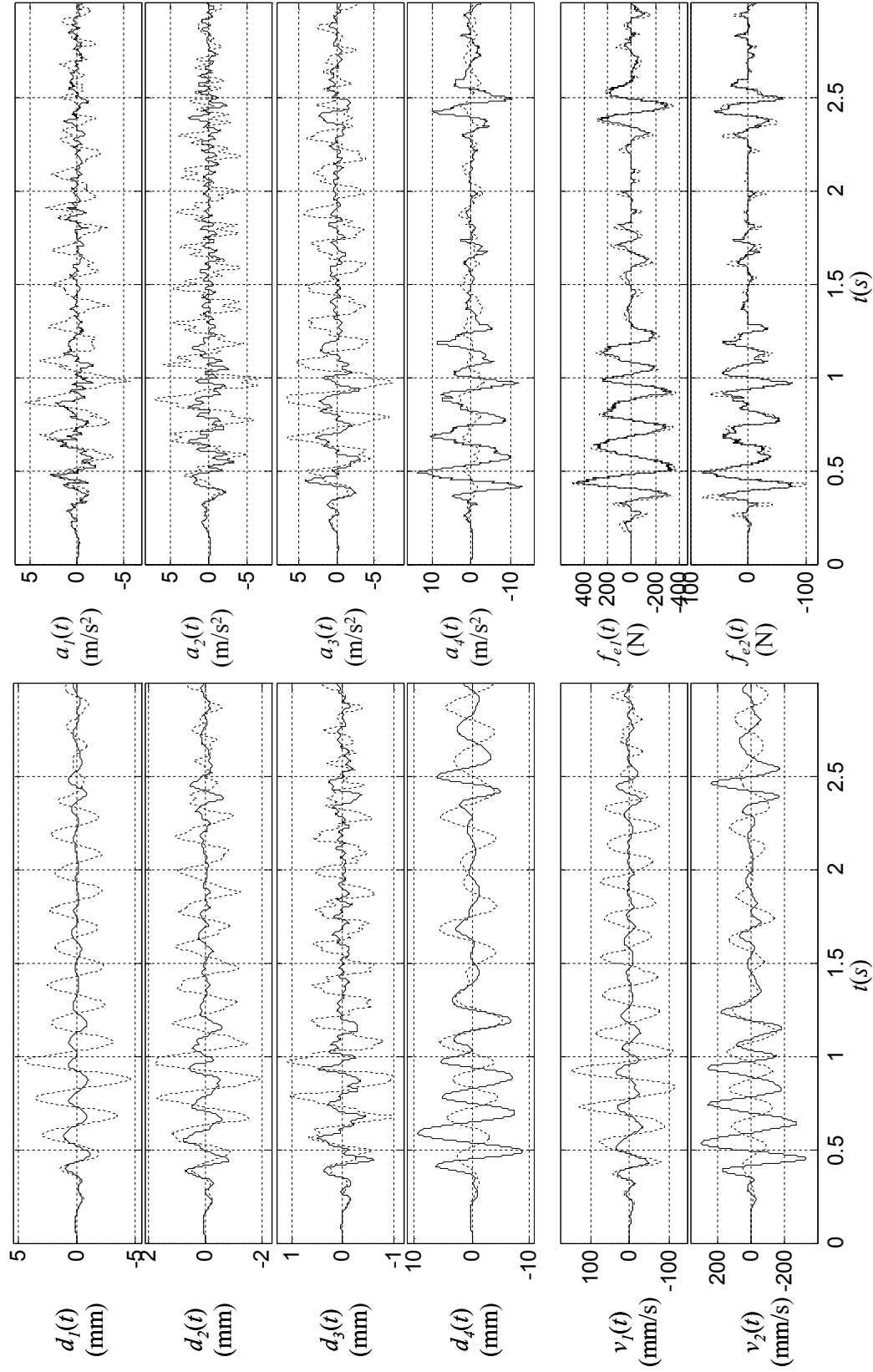


Figure 7.8a: Mechanical response quantities for El Centro earthquake with CZ control

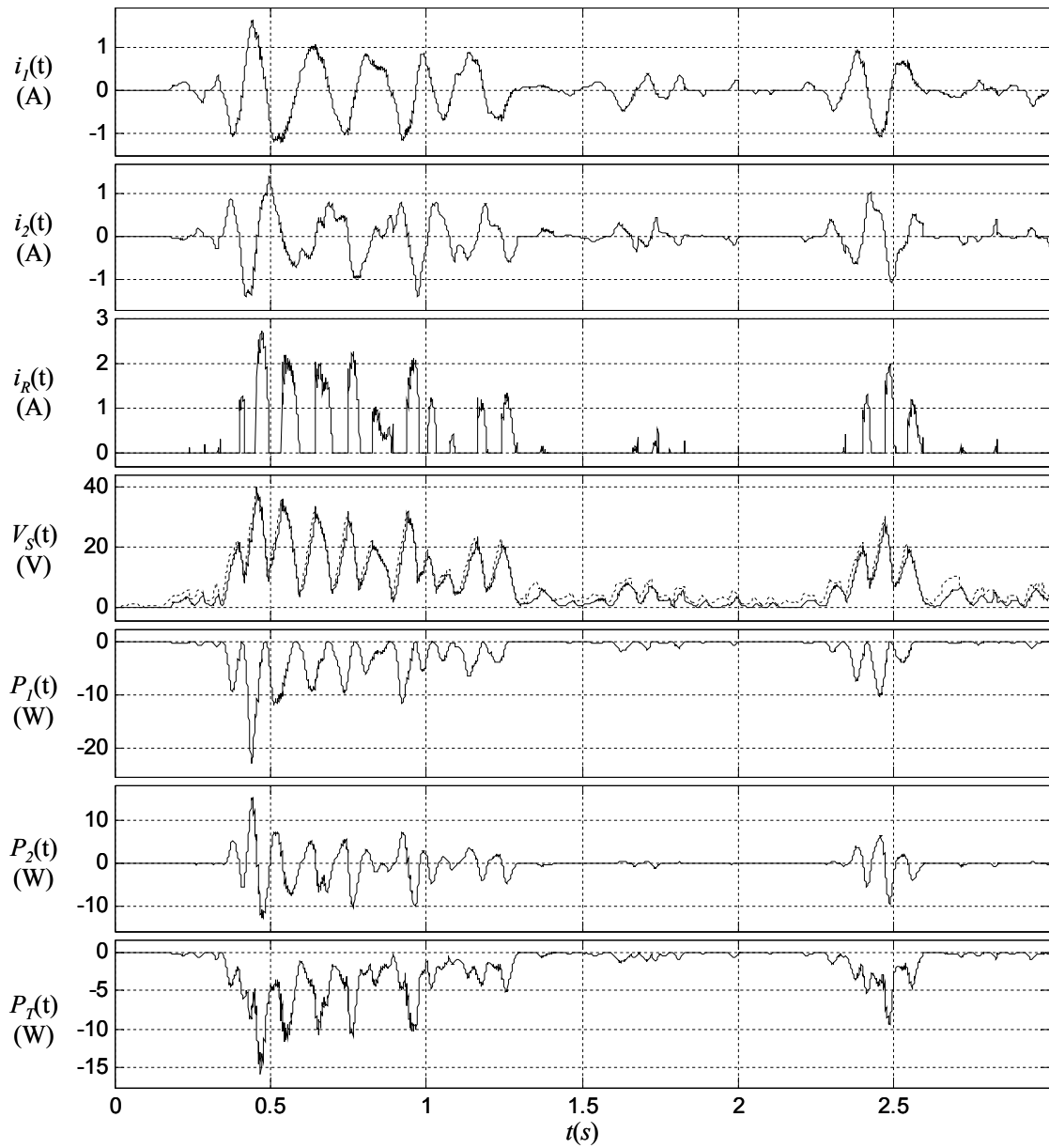


Figure 7.8b: Electrical response quantities for El Centro earthquake with CZ control

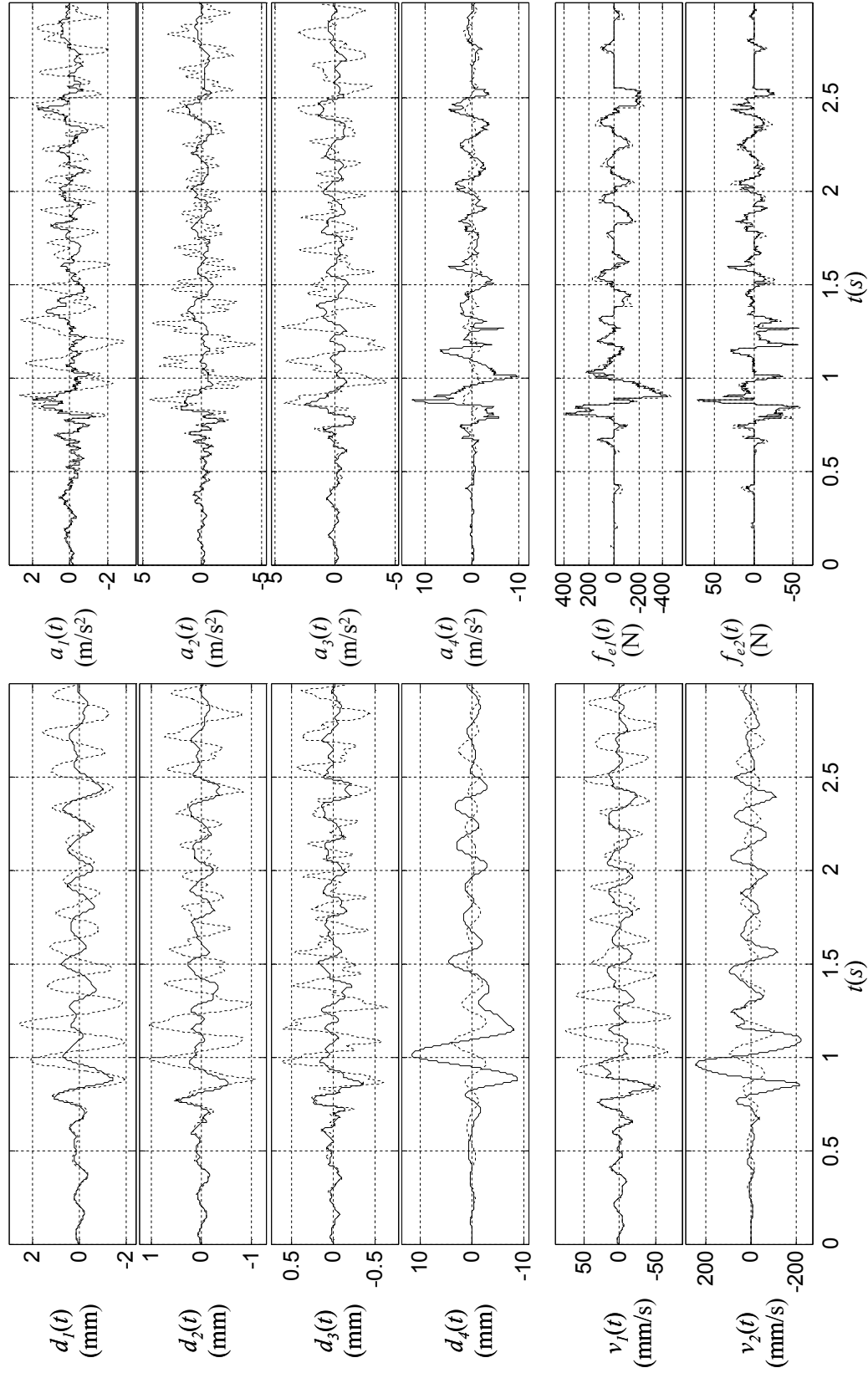


Figure 7.9a: Mechanical response quantities for Hachinohe earthquake with CO control

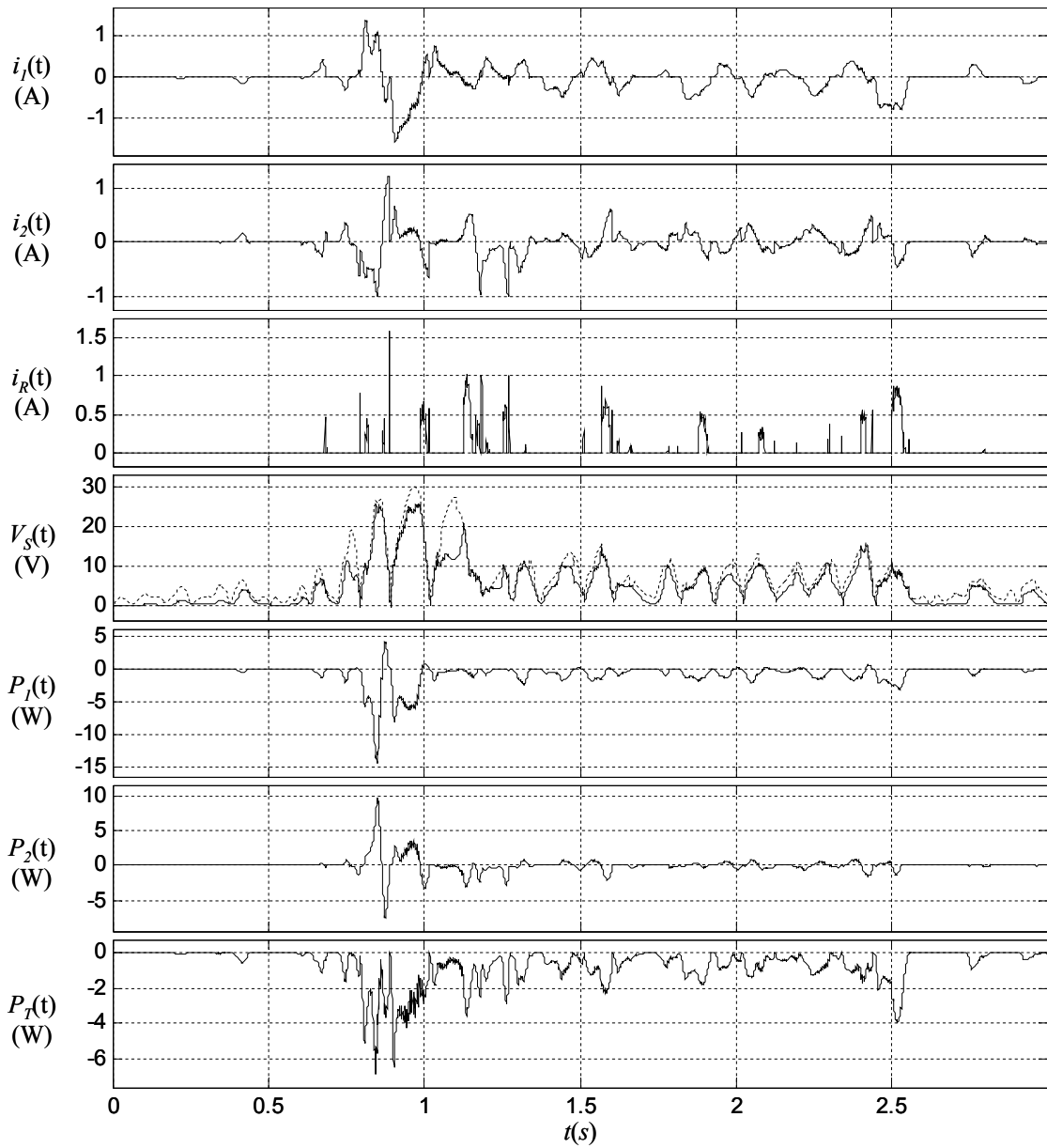


Figure 7.9b: Electrical response quantities for Hachinohe earthquake with CO control

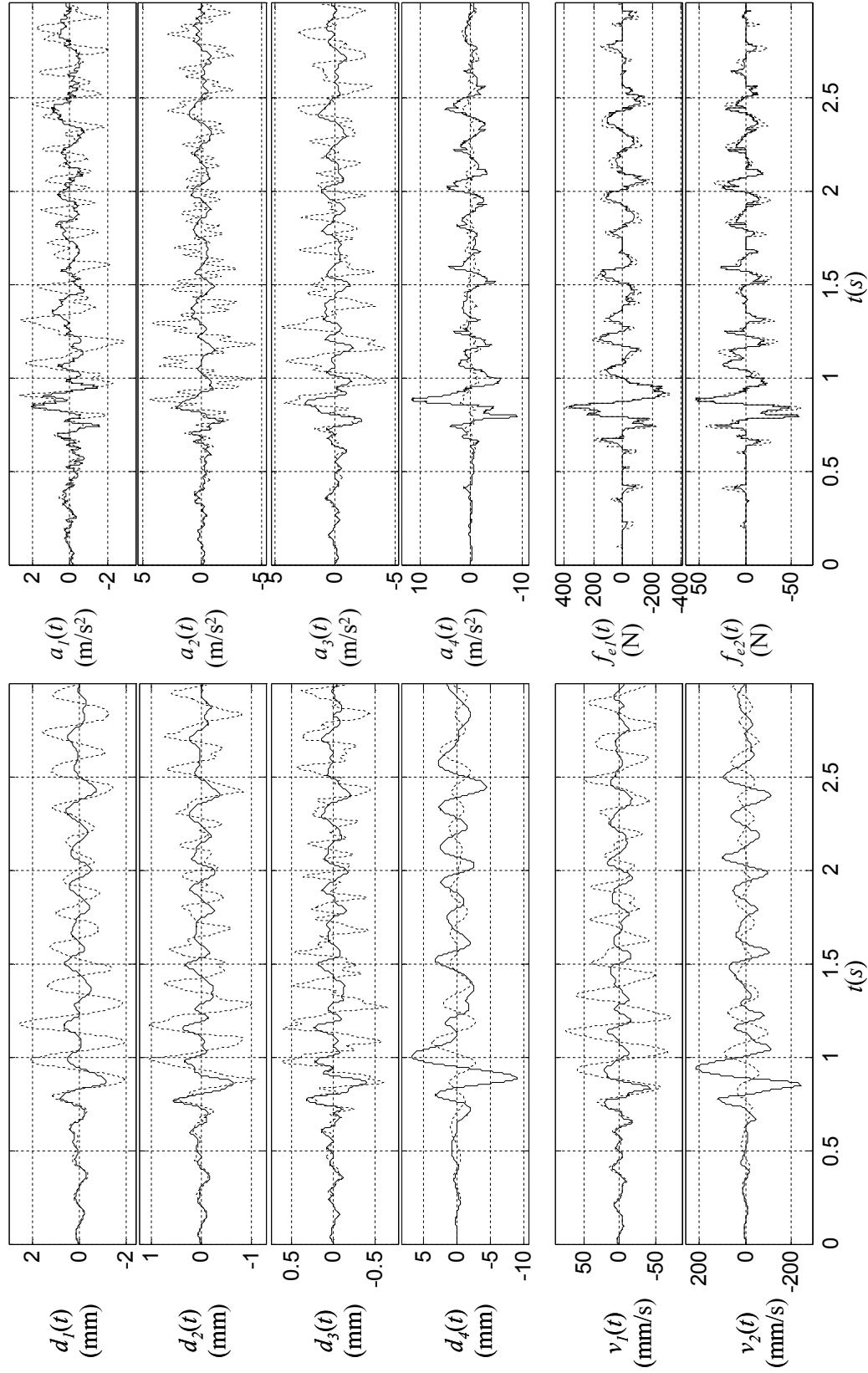


Figure 7.10a: Mechanical response quantities for Hachinohe earthquake with DR-S control

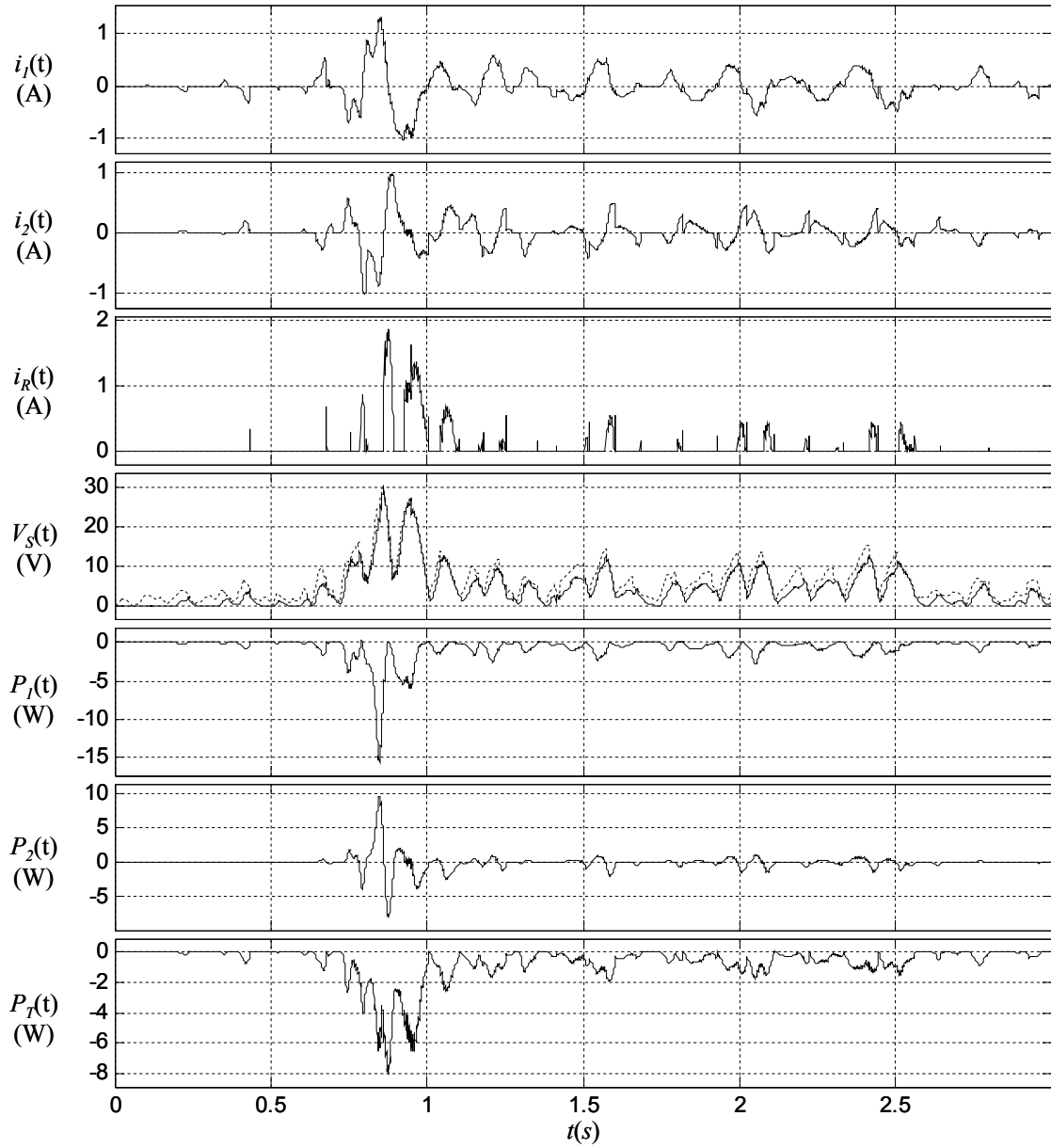
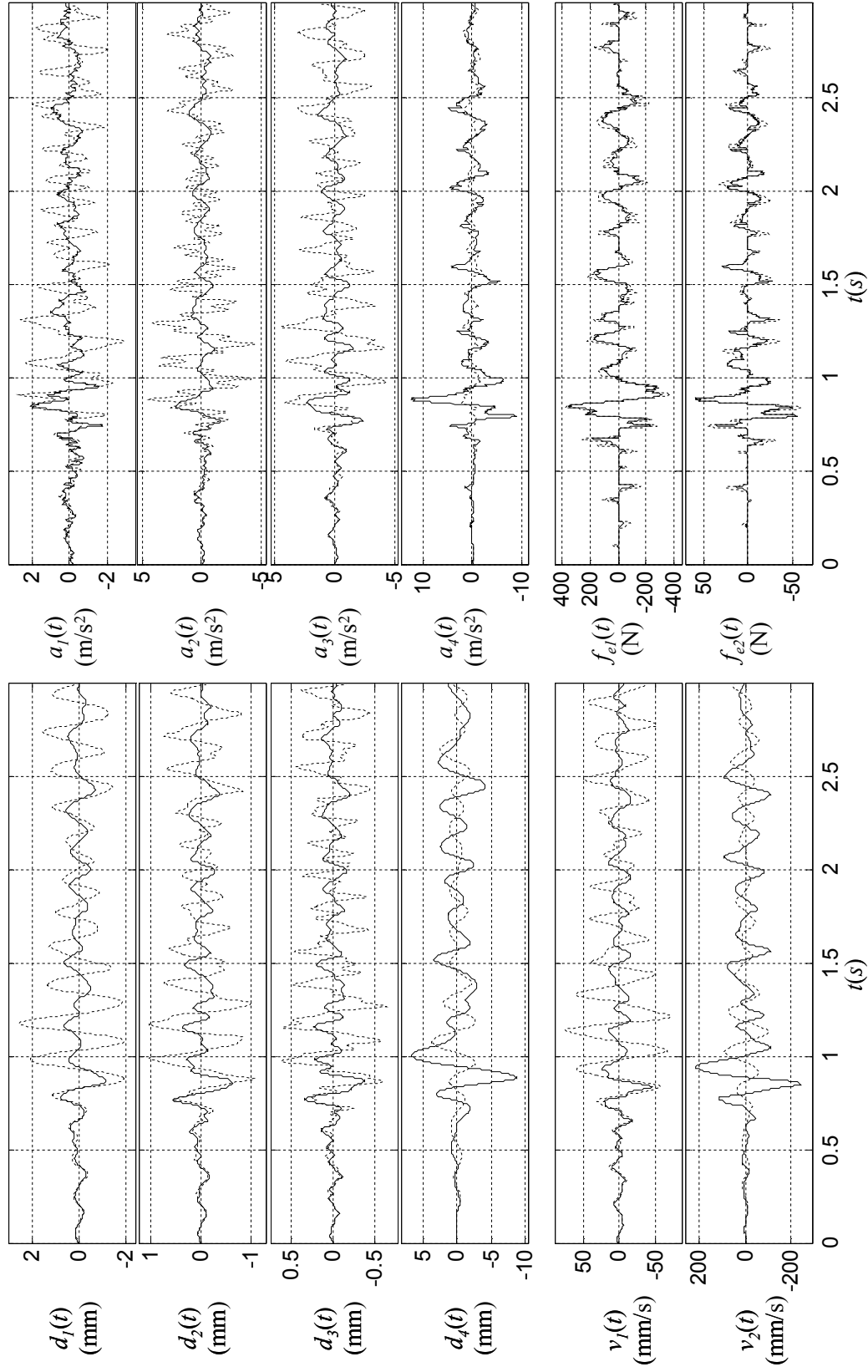


Figure 7.10b: Electrical response quantities for Hachinohe earthquake with DR-S control

Figure 7.1.1a: Mechanical response quantities for Hachinohe earthquake with DR- \mathcal{H}_∞ control

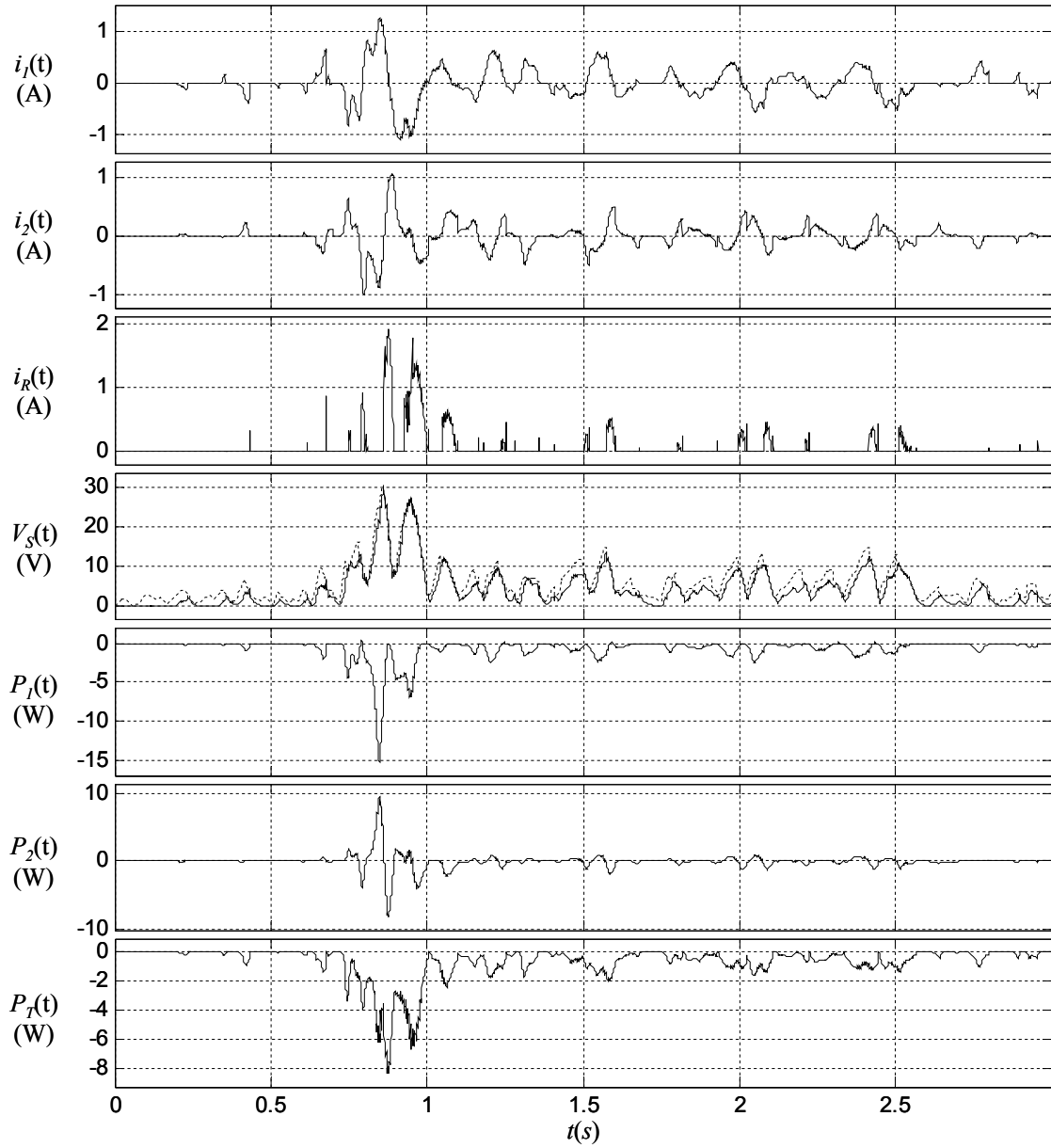


Figure 7.11b: Electrical response quantities for Hachinohe earthquake with DR- \mathcal{H}_∞ control

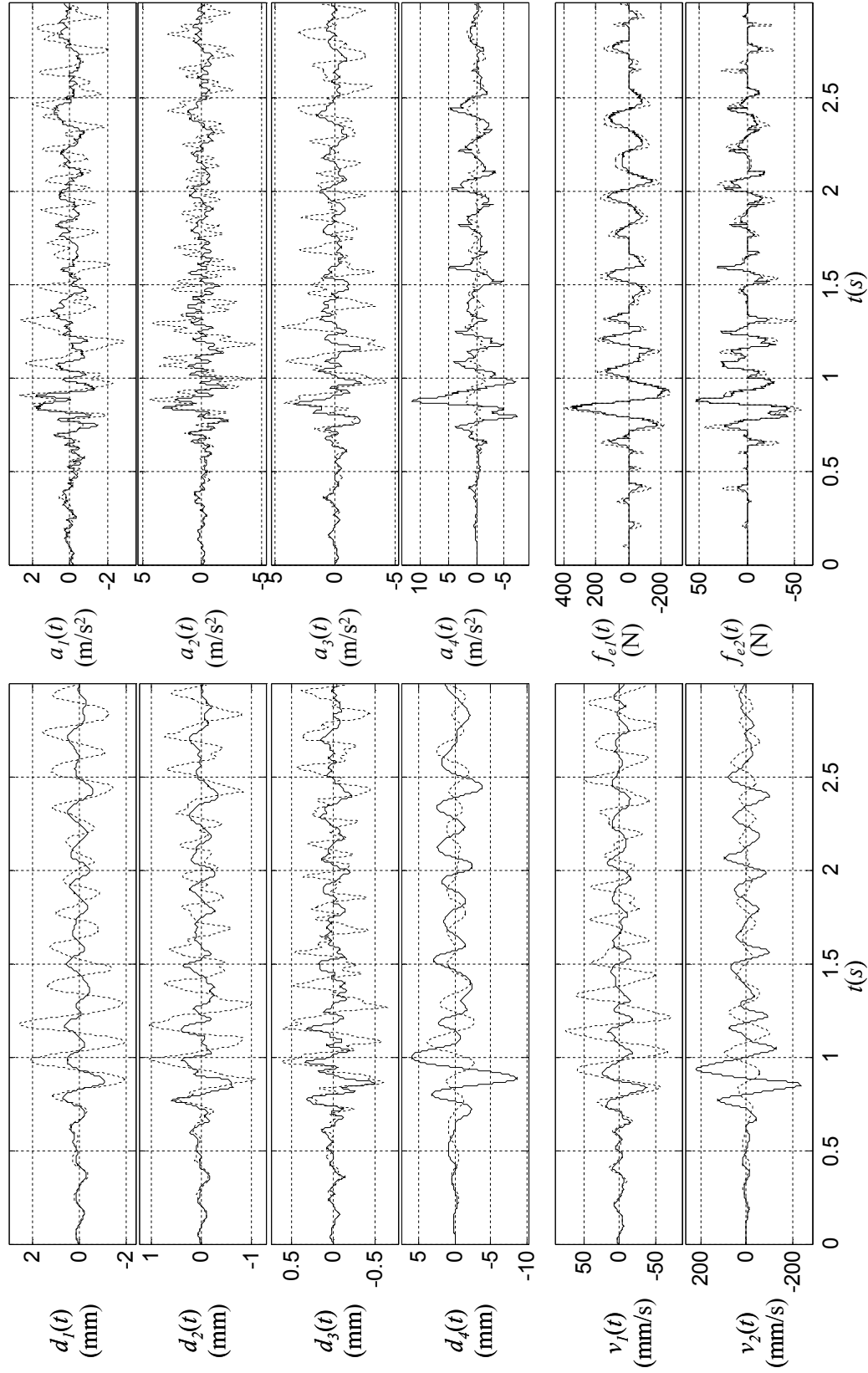


Figure 7.12a: Mechanical response quantities for Hachinohe earthquake with CZ control

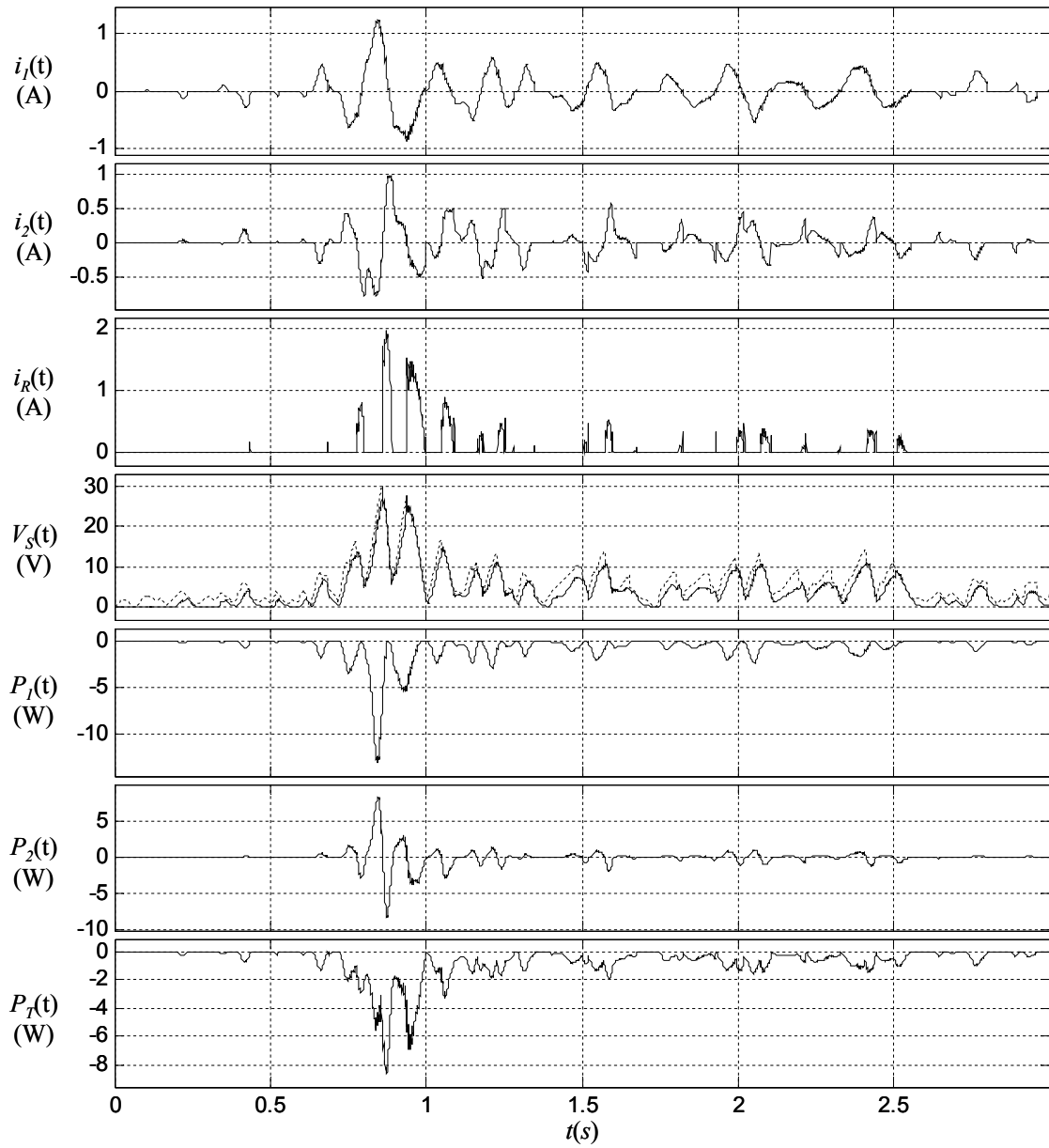


Figure 7.12b: Electrical response quantities for Hachinohe earthquake with CZ control

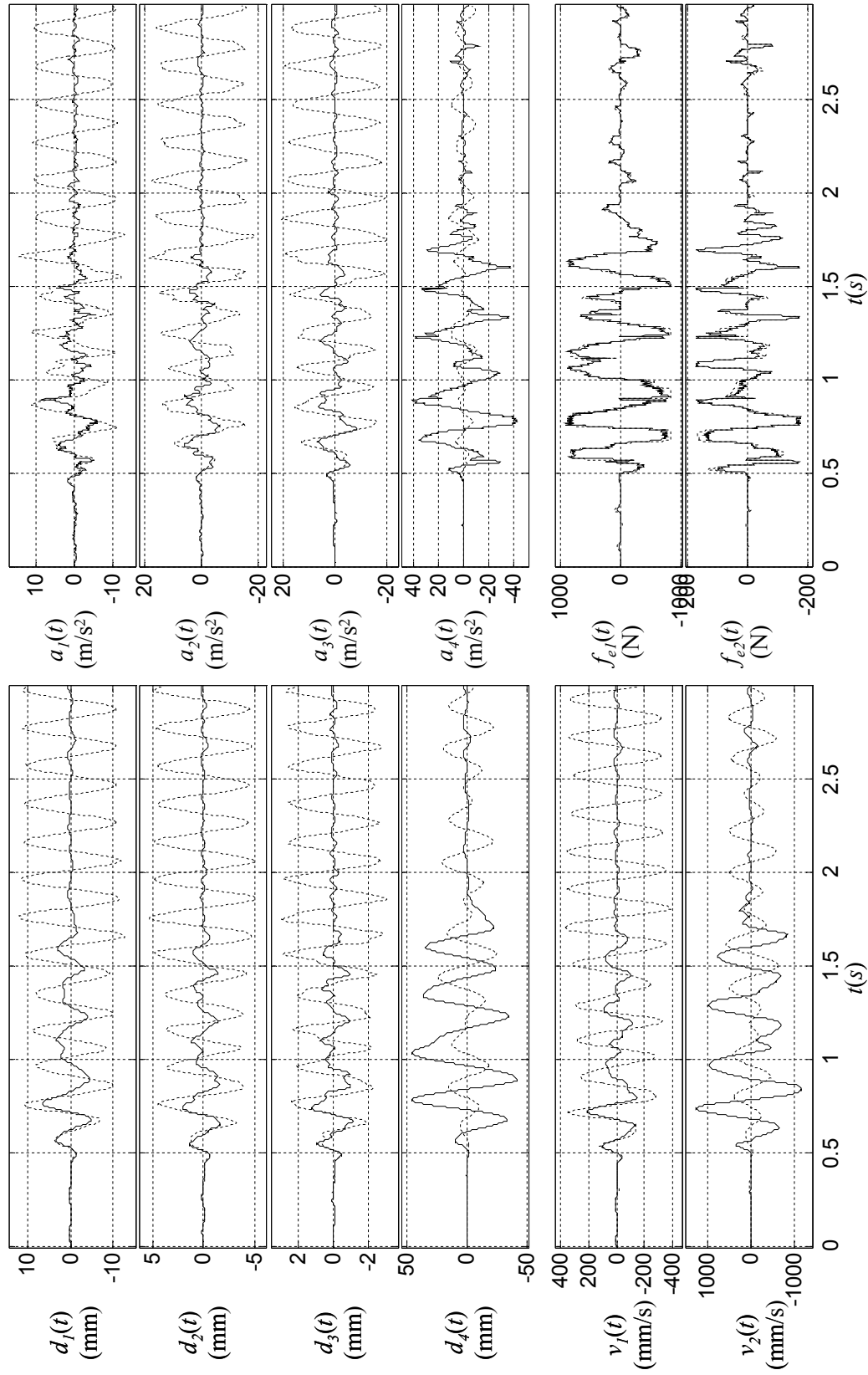


Figure 7.13a: Mechanical response quantities for Kobe earthquake with CO control

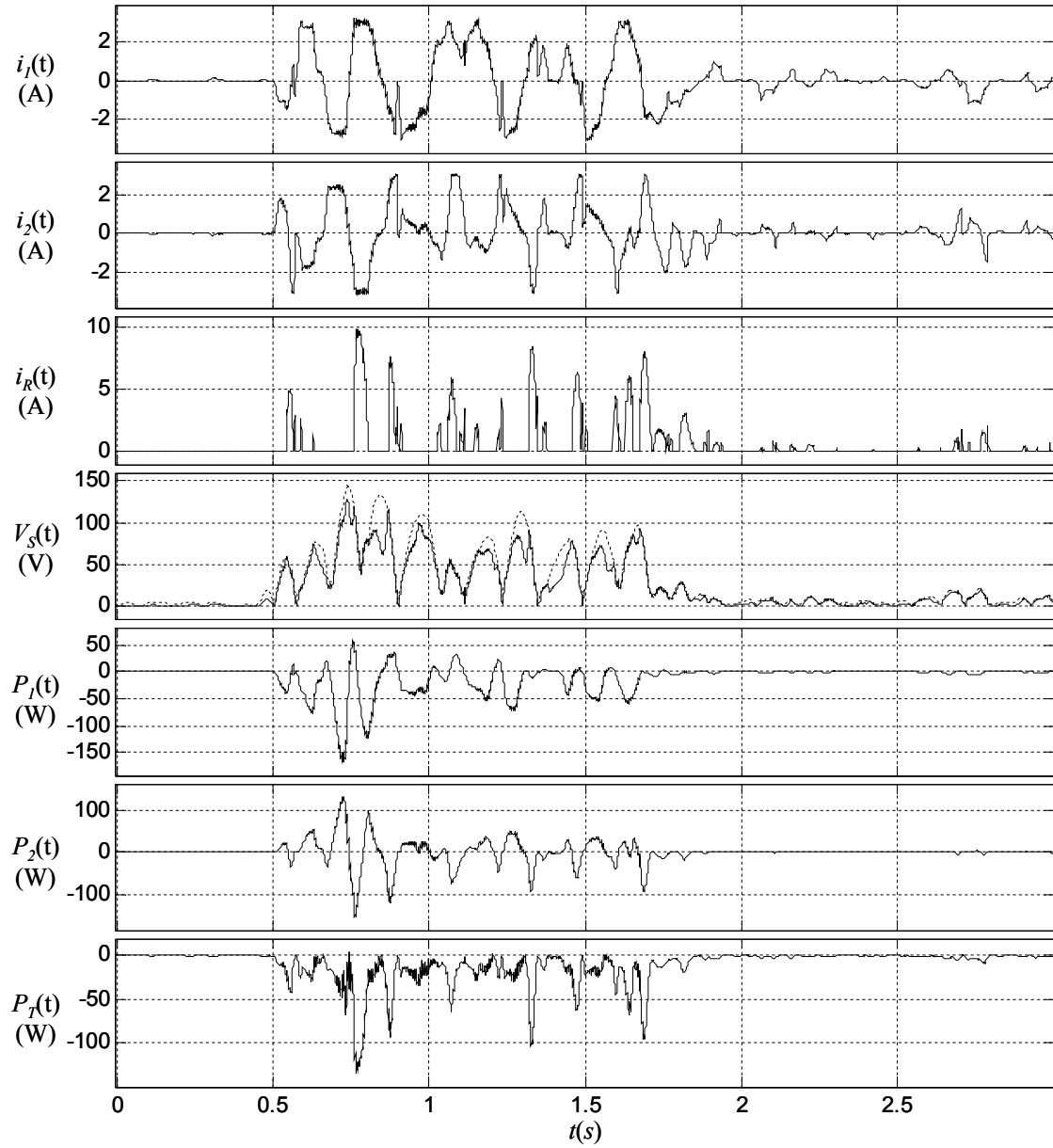


Figure 7.13b: Electrical response quantities for Kobe earthquake with CO control

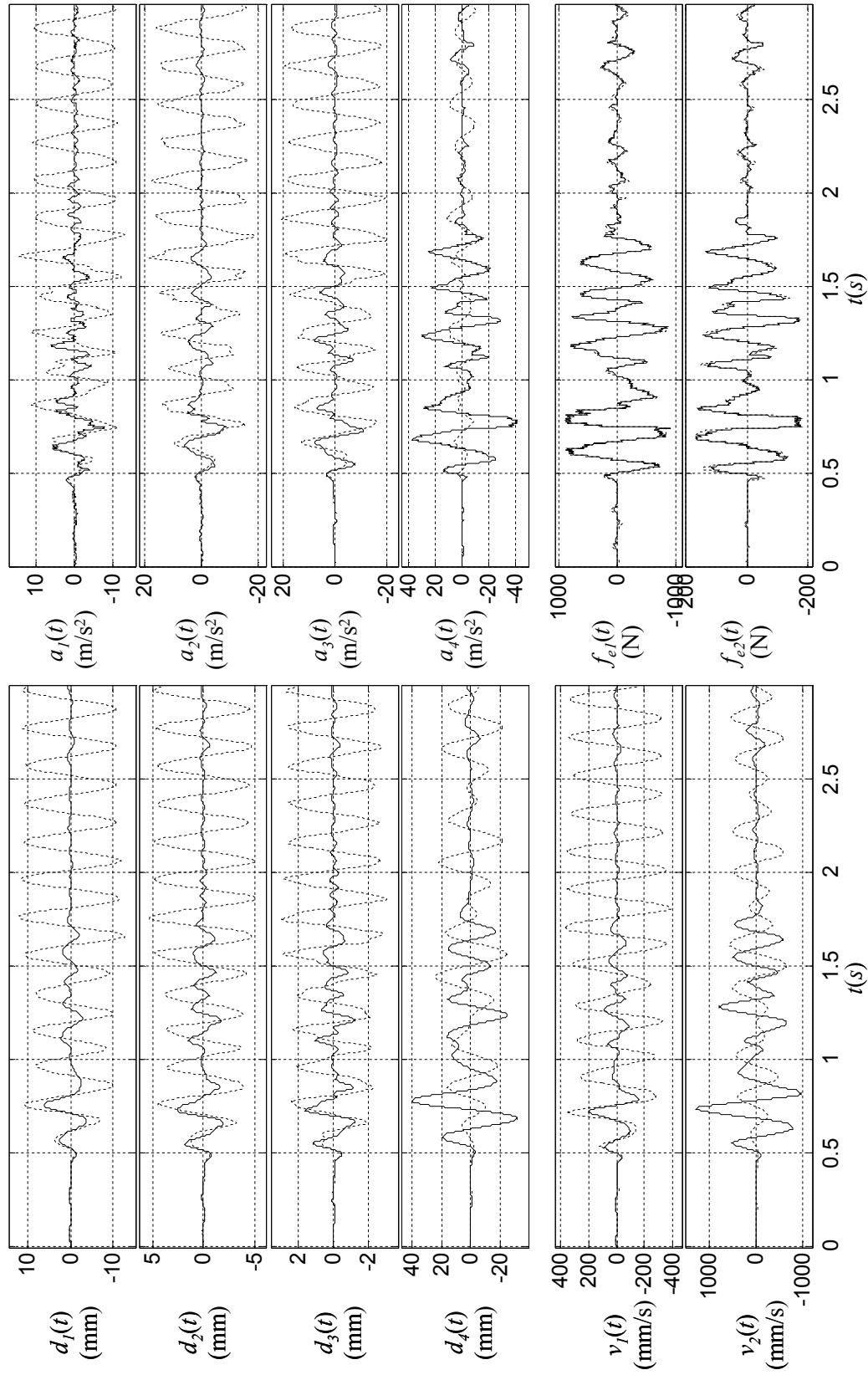


Figure 7.14a: Mechanical response quantities for Kobe earthquake with DR-S control

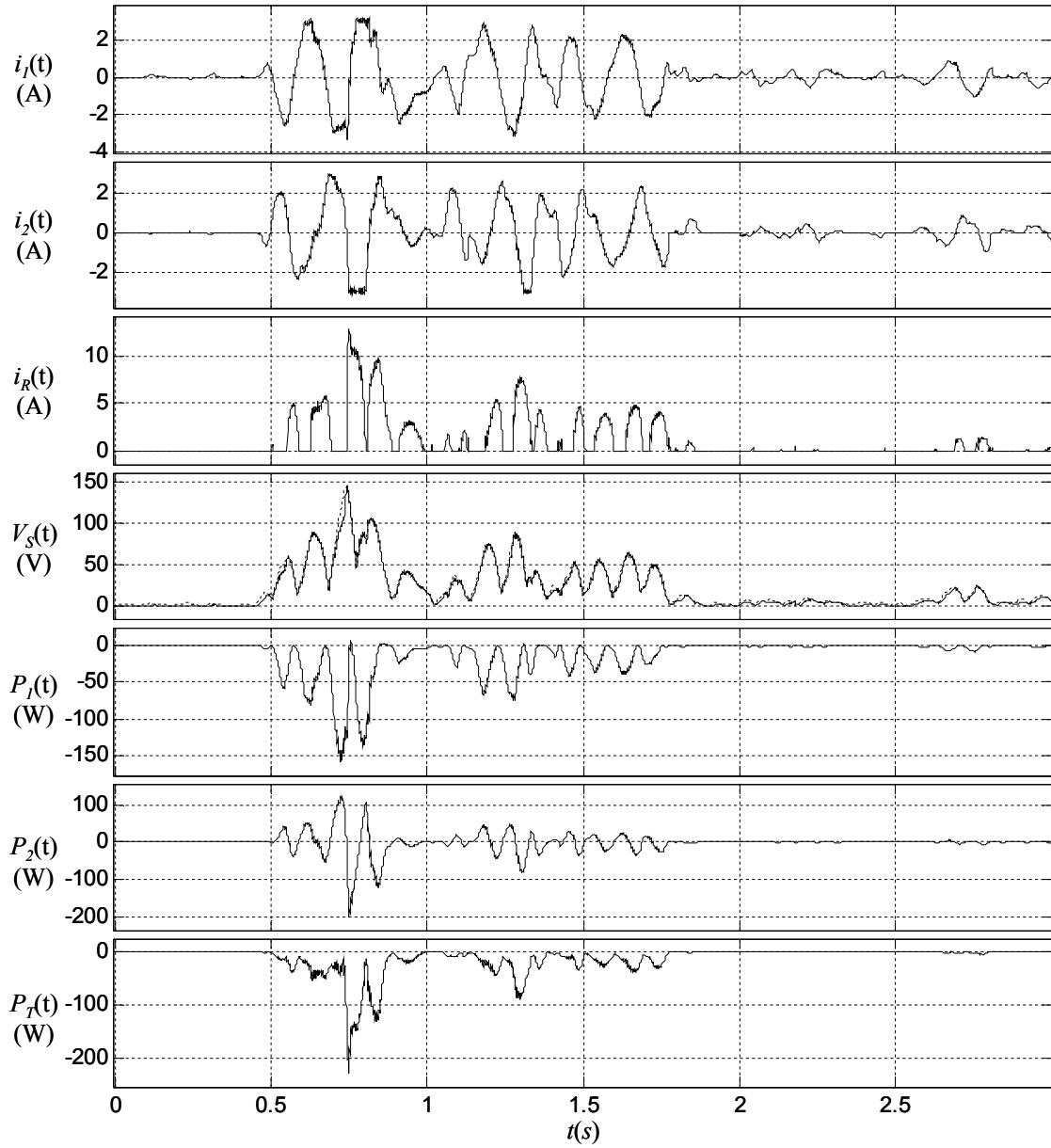
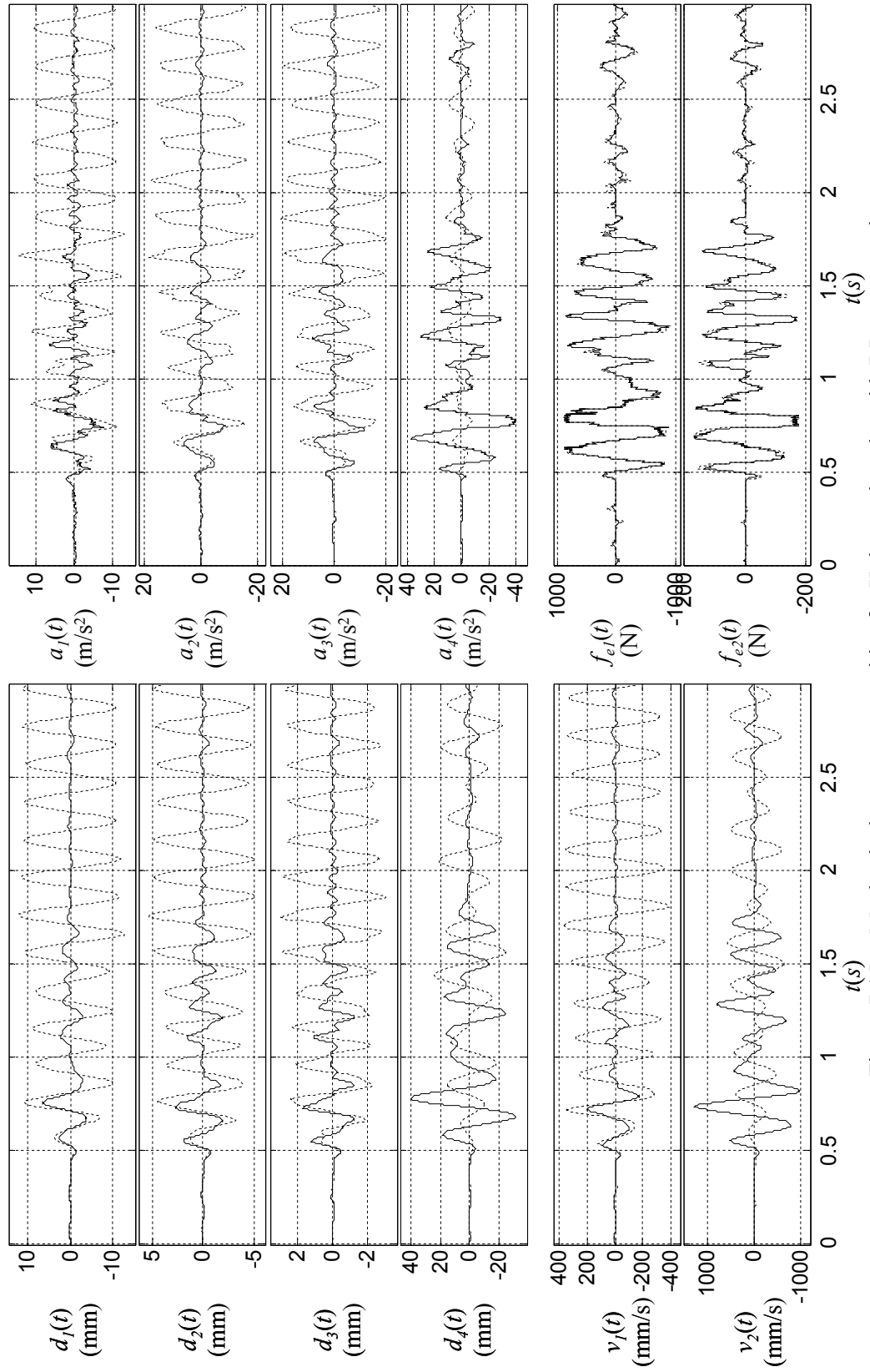


Figure 7.14b: Electrical response quantities for Kobe earthquake with DR-S control

Figure 7.15a: Mechanical response quantities for Kobe earthquake with DR- \mathcal{F}_c control

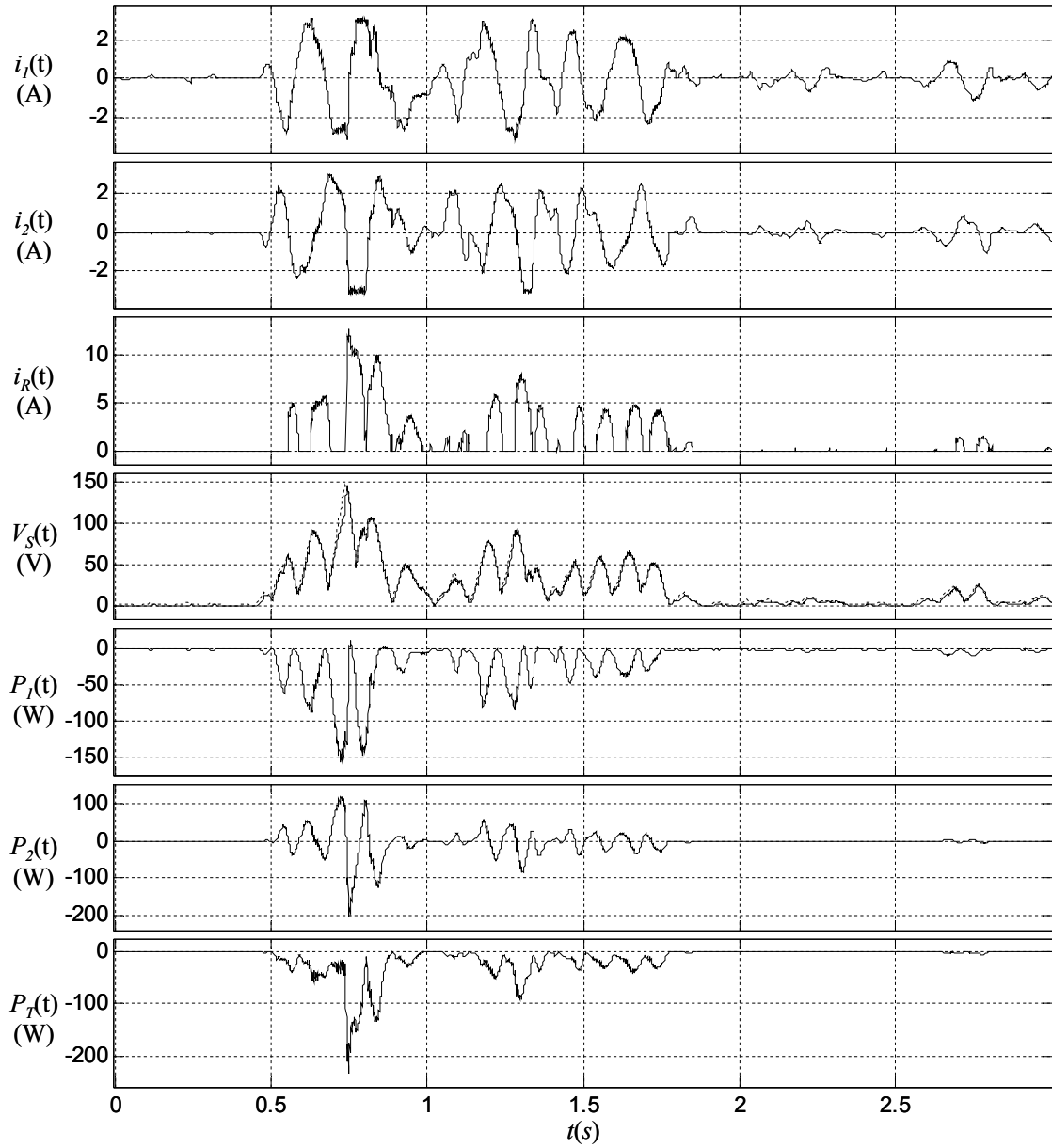


Figure 7.15b: Electrical response quantities for Kobe earthquake with DR- \mathcal{H}_∞ control

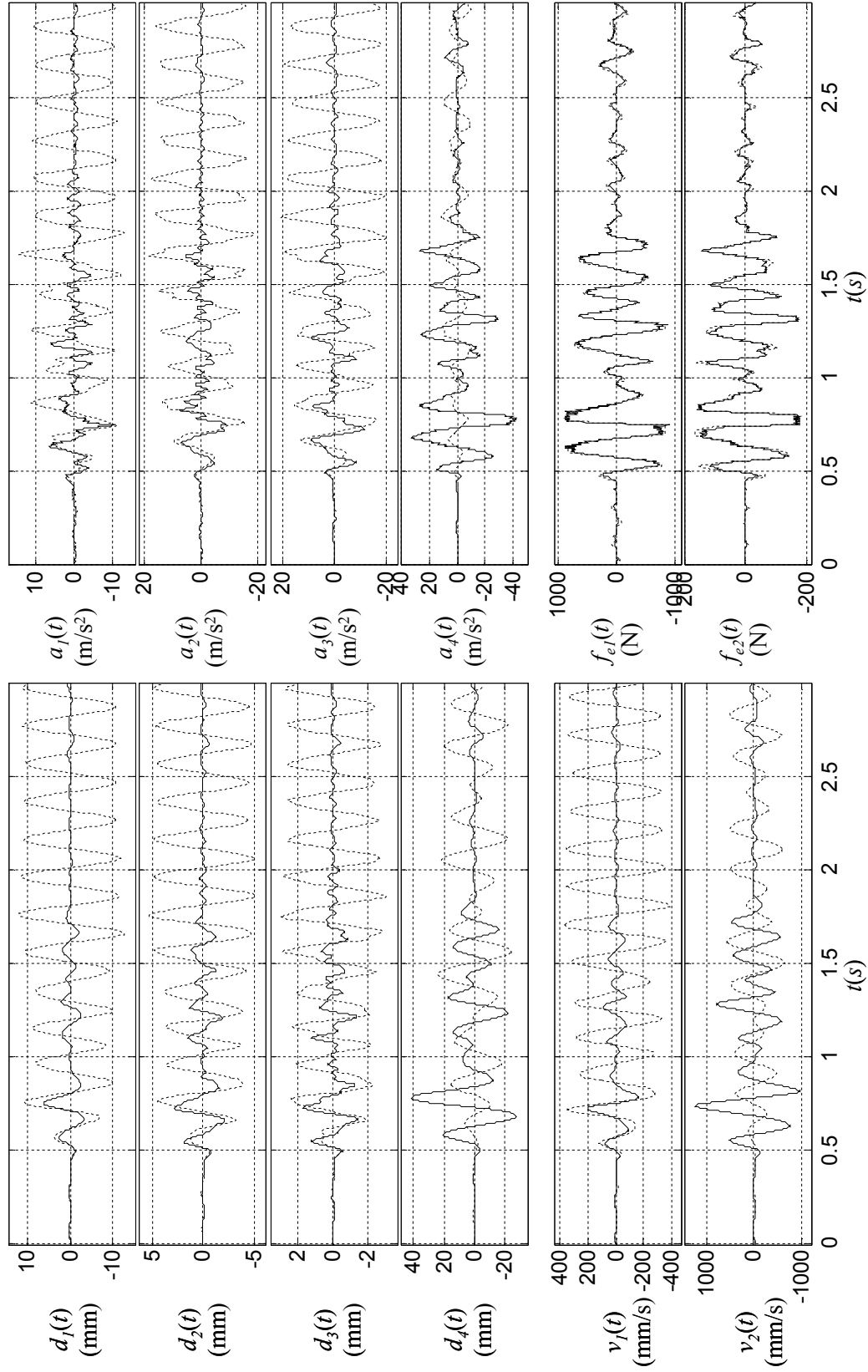


Figure 7.16a: Mechanical response quantities for Kobe earthquake with CZ control

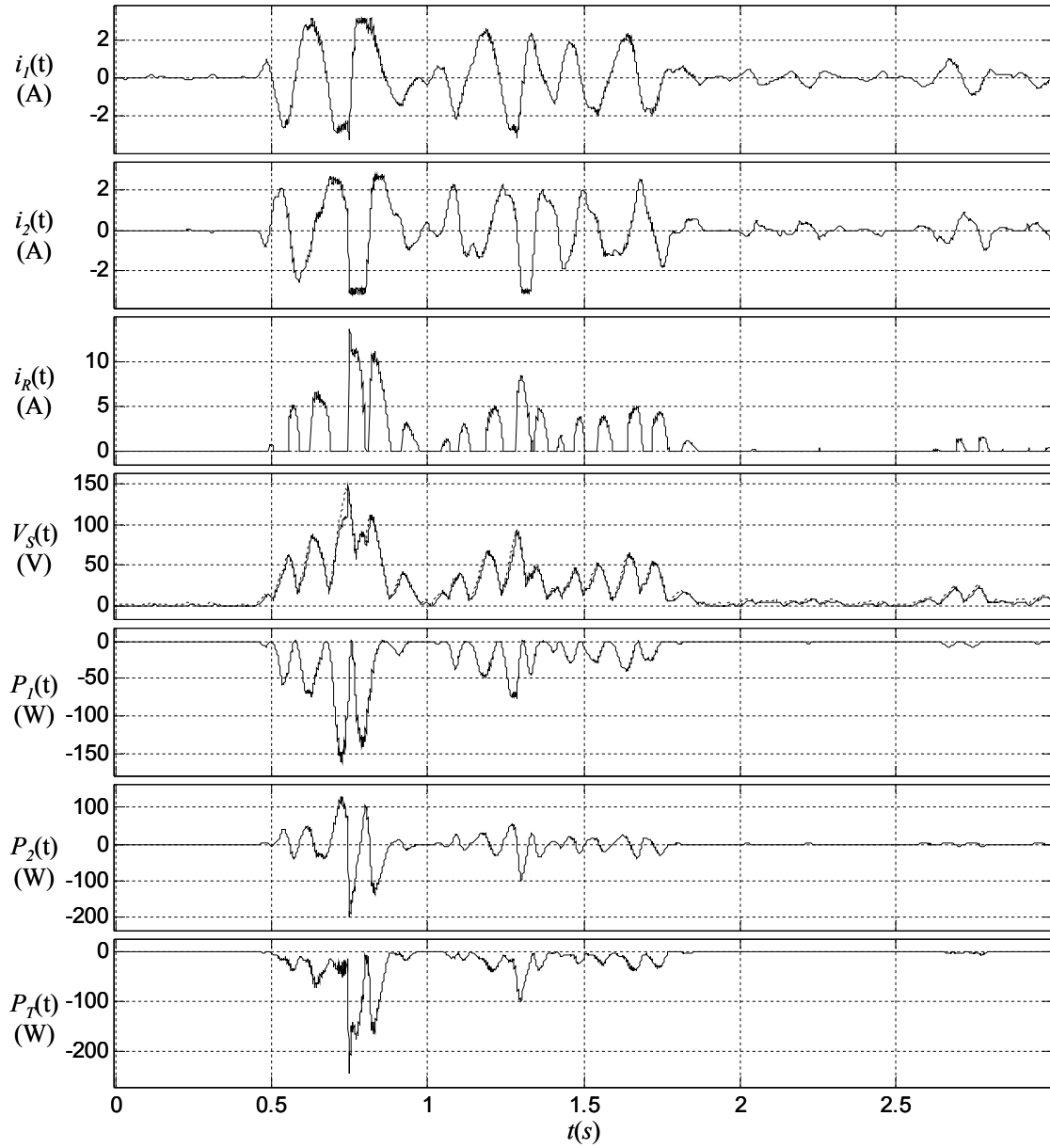


Figure 7.16b: Electrical response quantities for Kobe earthquake with CZ control

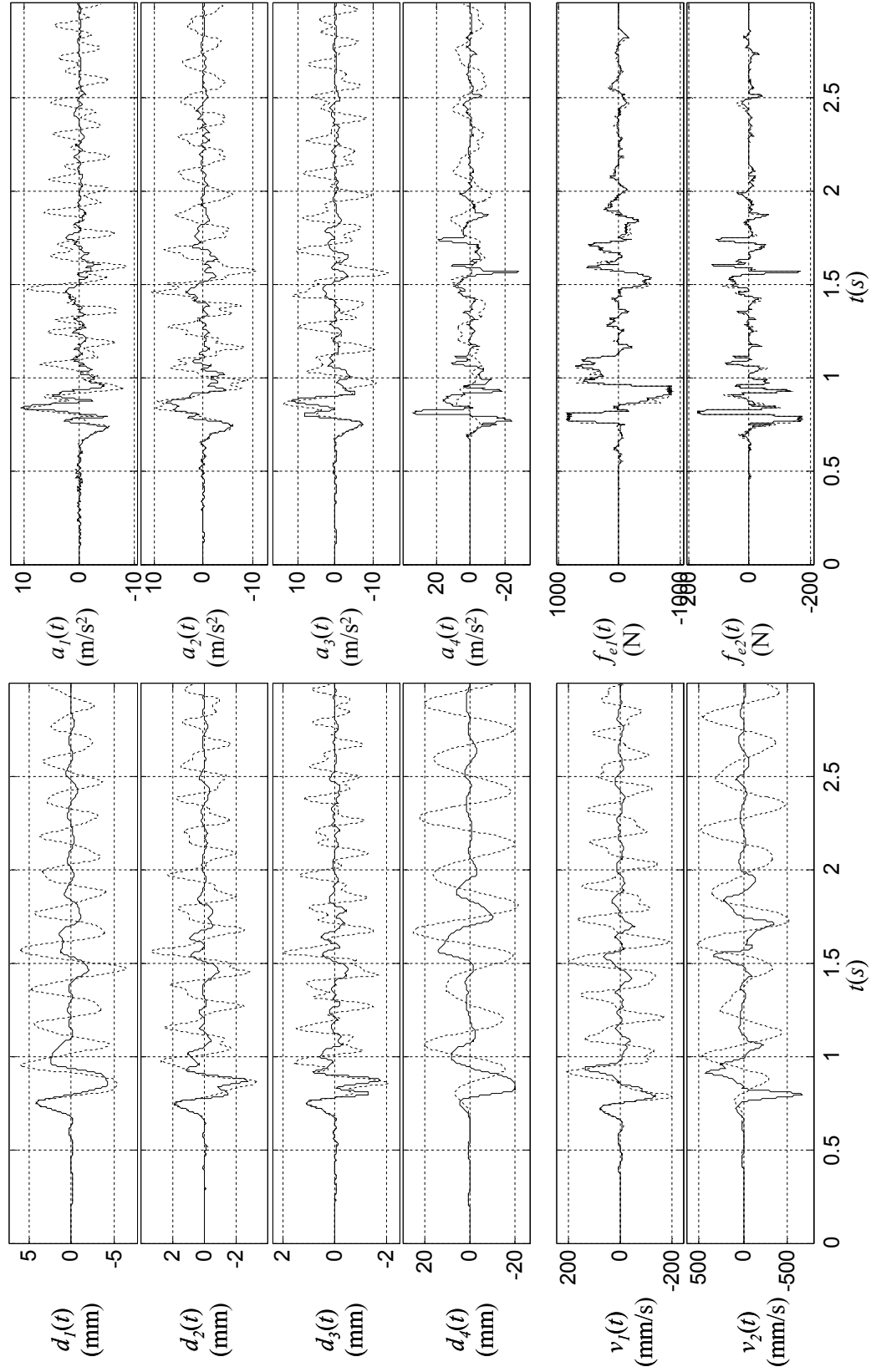


Figure 7.17a: Mechanical response quantities for Northridge earthquake with CO control

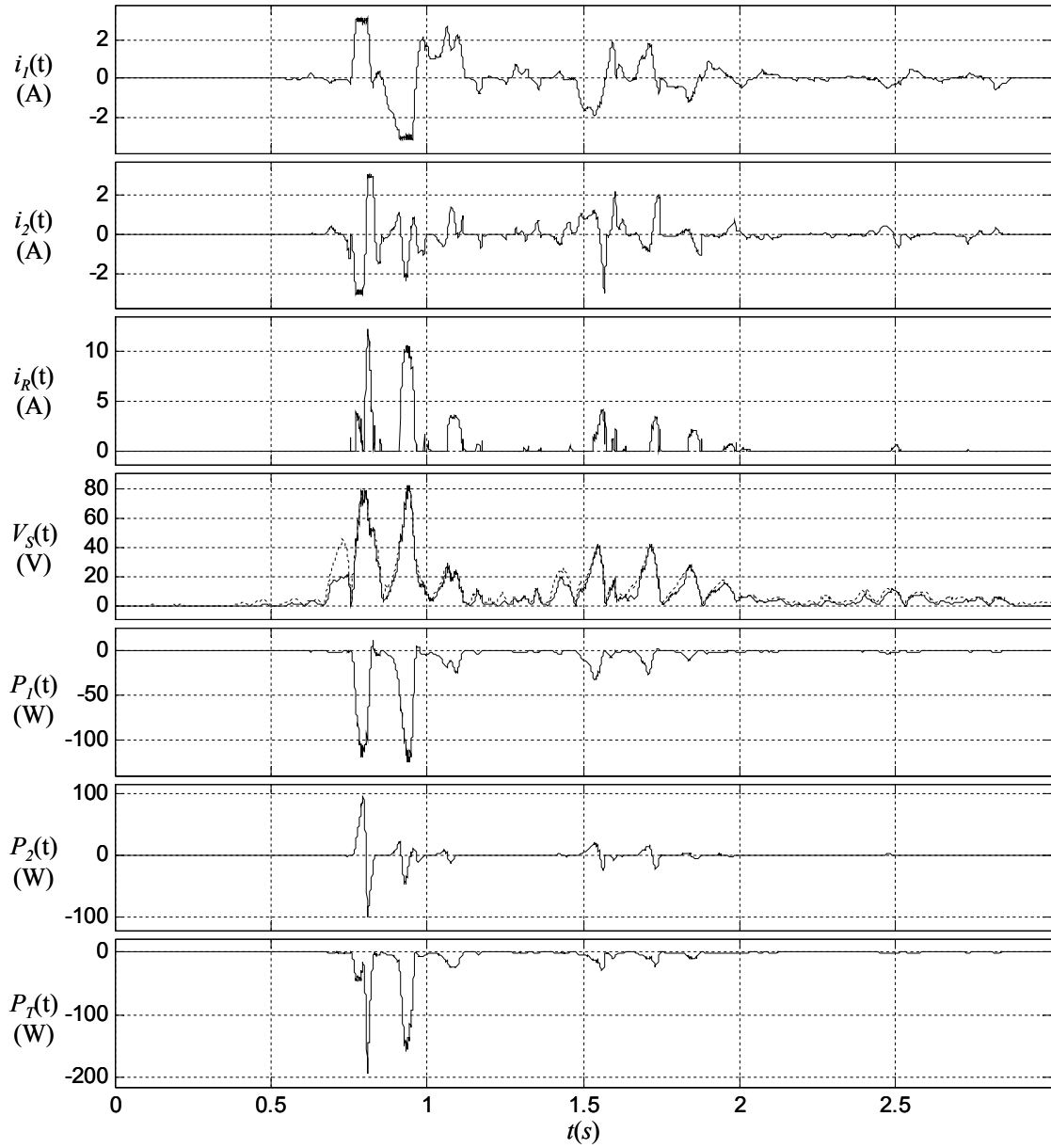


Figure 7.17b: Electrical response quantities for Northridge earthquake with CO control

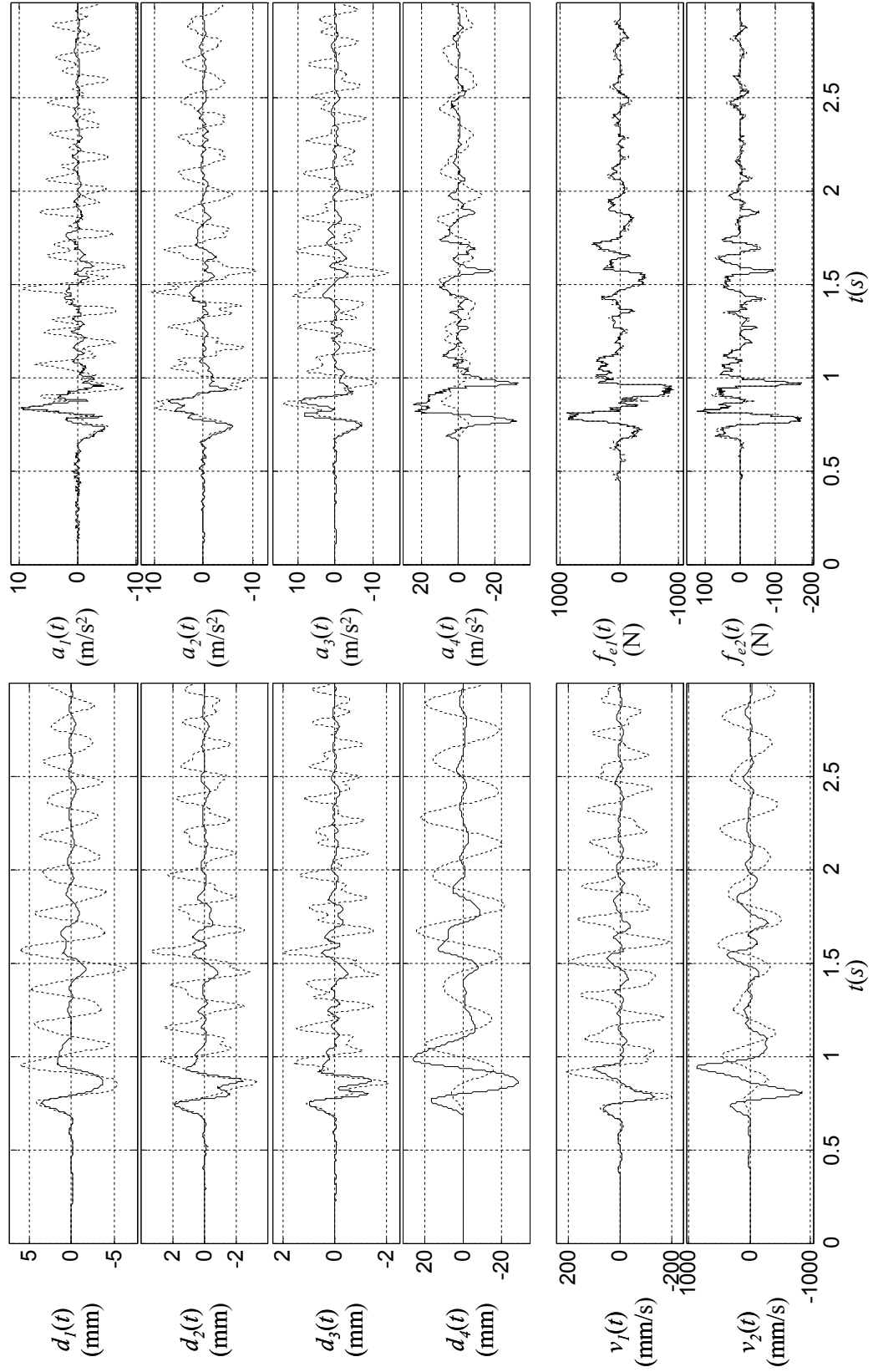


Figure 7.18a: Mechanical response quantities for Northridge earthquake with DR-S control

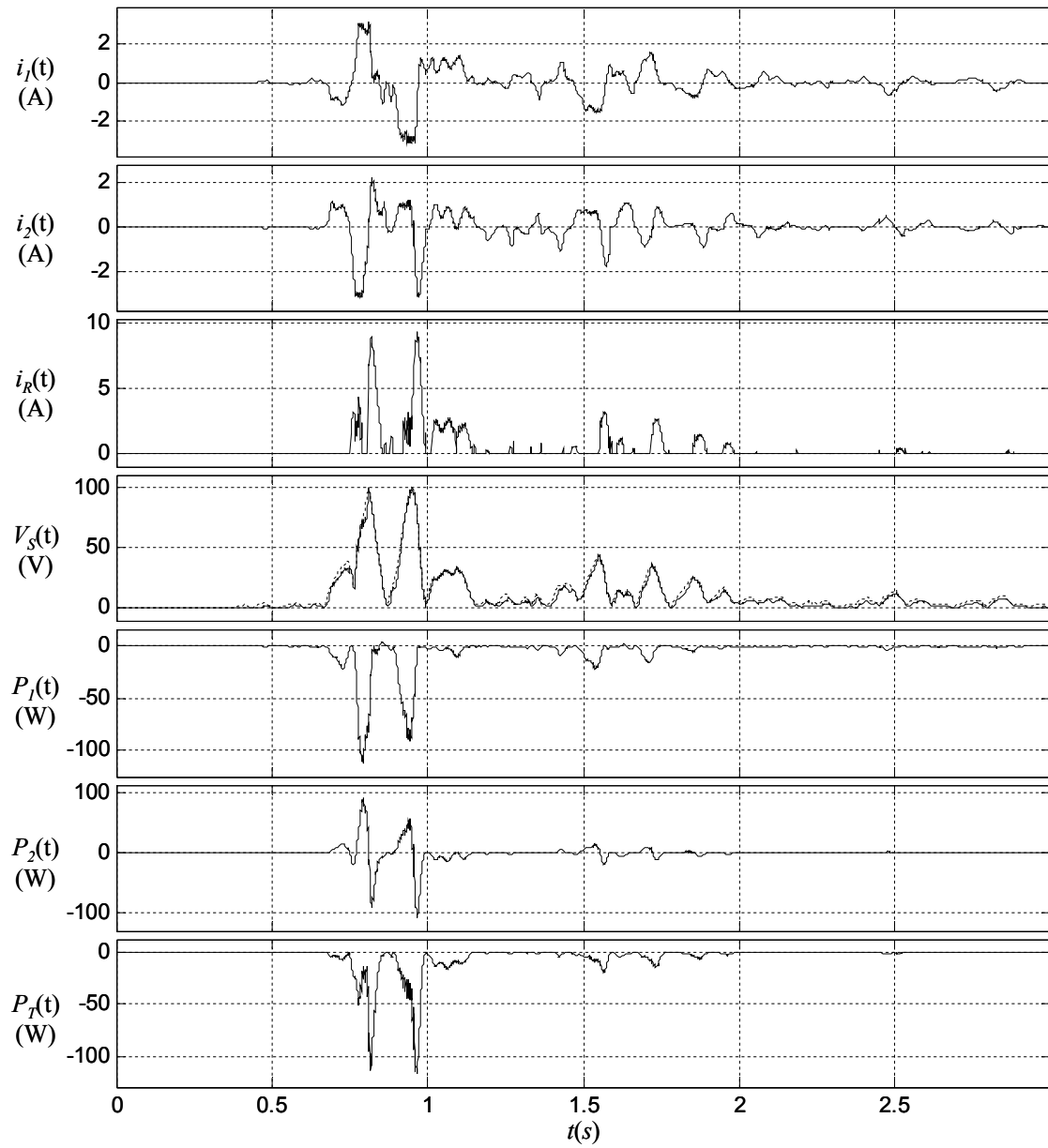
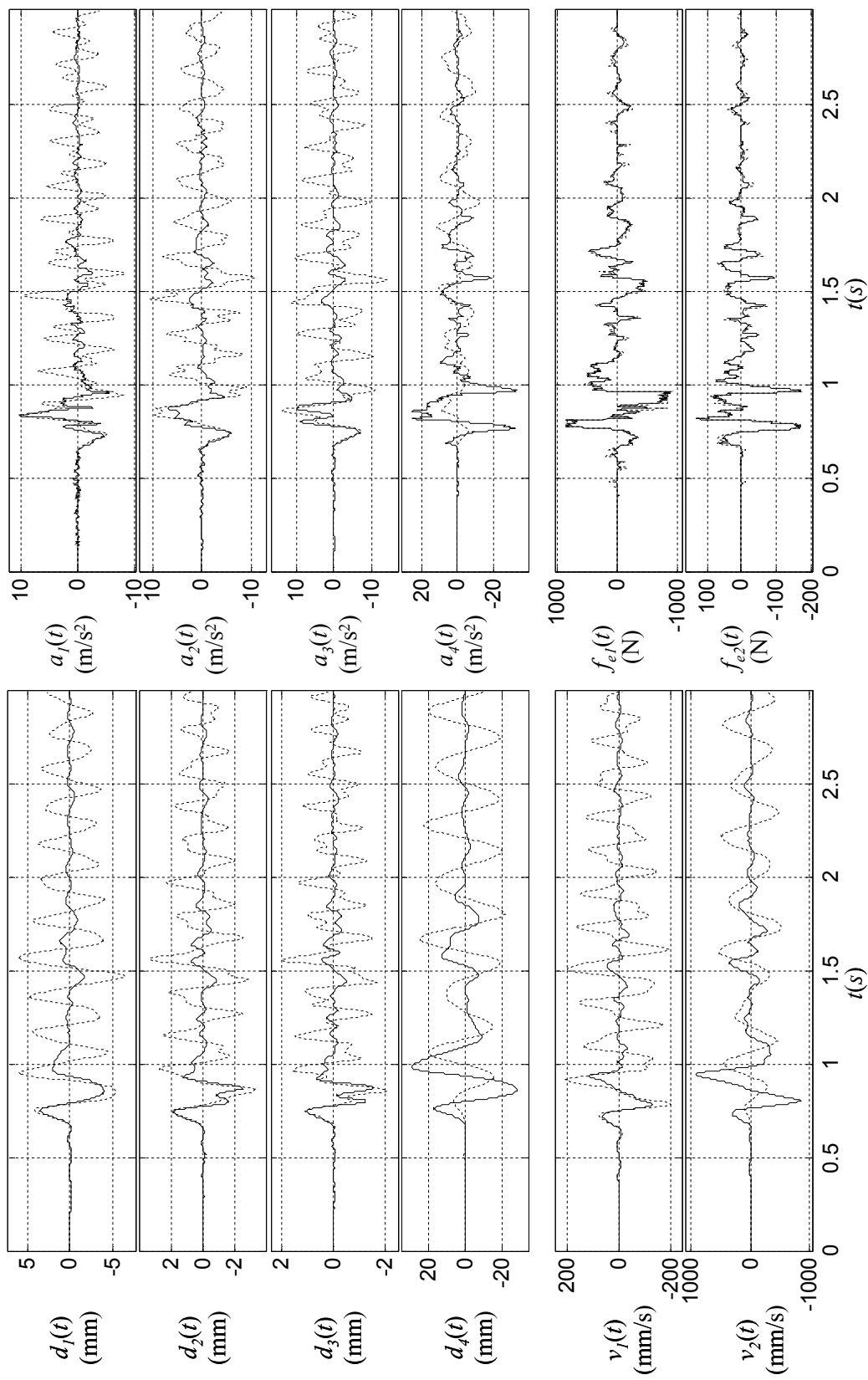


Figure 7.18b: Electrical response quantities for Northridge earthquake with DR-S control

Figure 7.19a: Mechanical response quantities for Northridge earthquake with DR- \mathcal{H}_∞ control

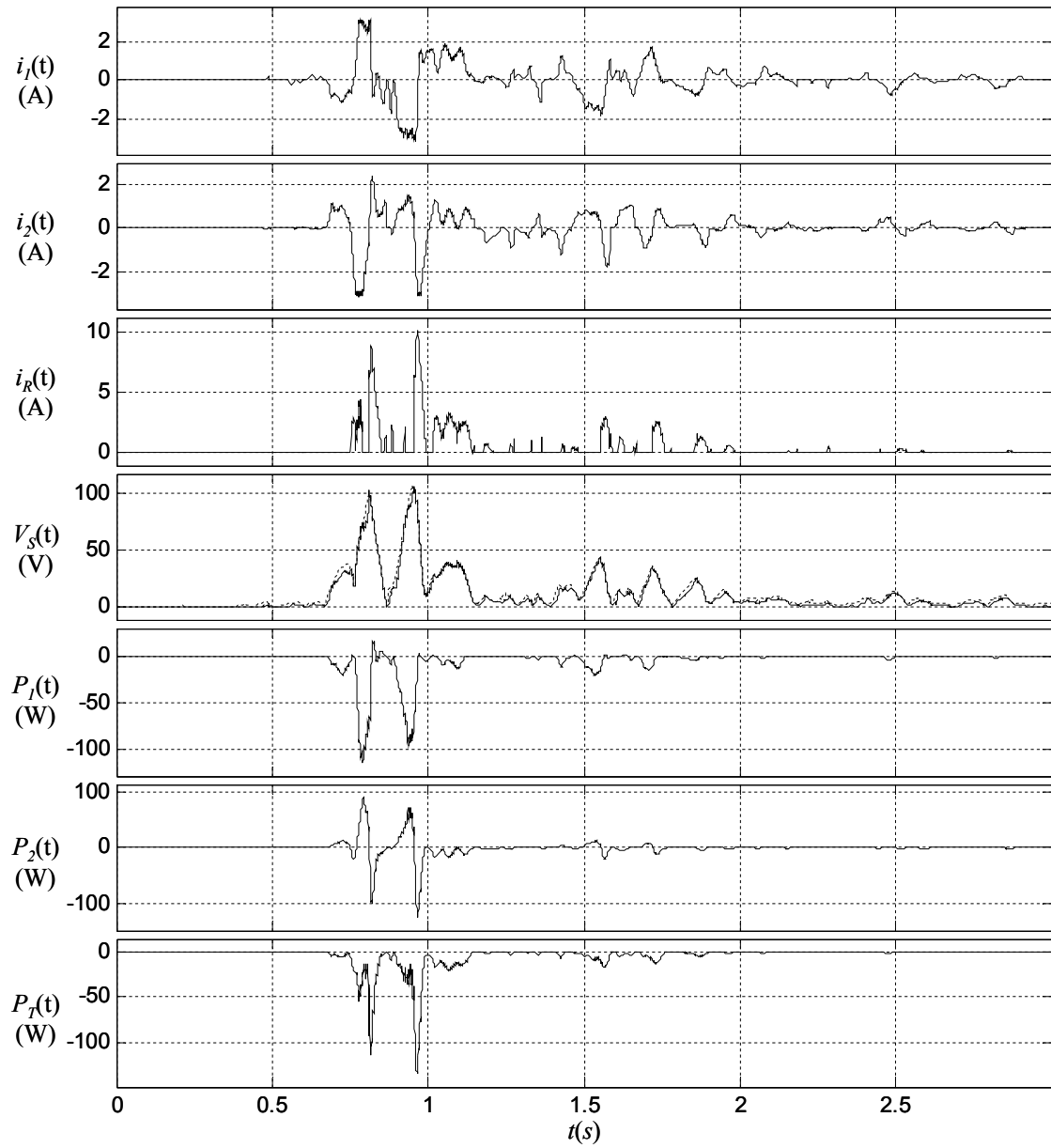


Figure 7.19b: Electrical response quantities for Northridge earthquake with DR- \mathcal{H}_∞ control

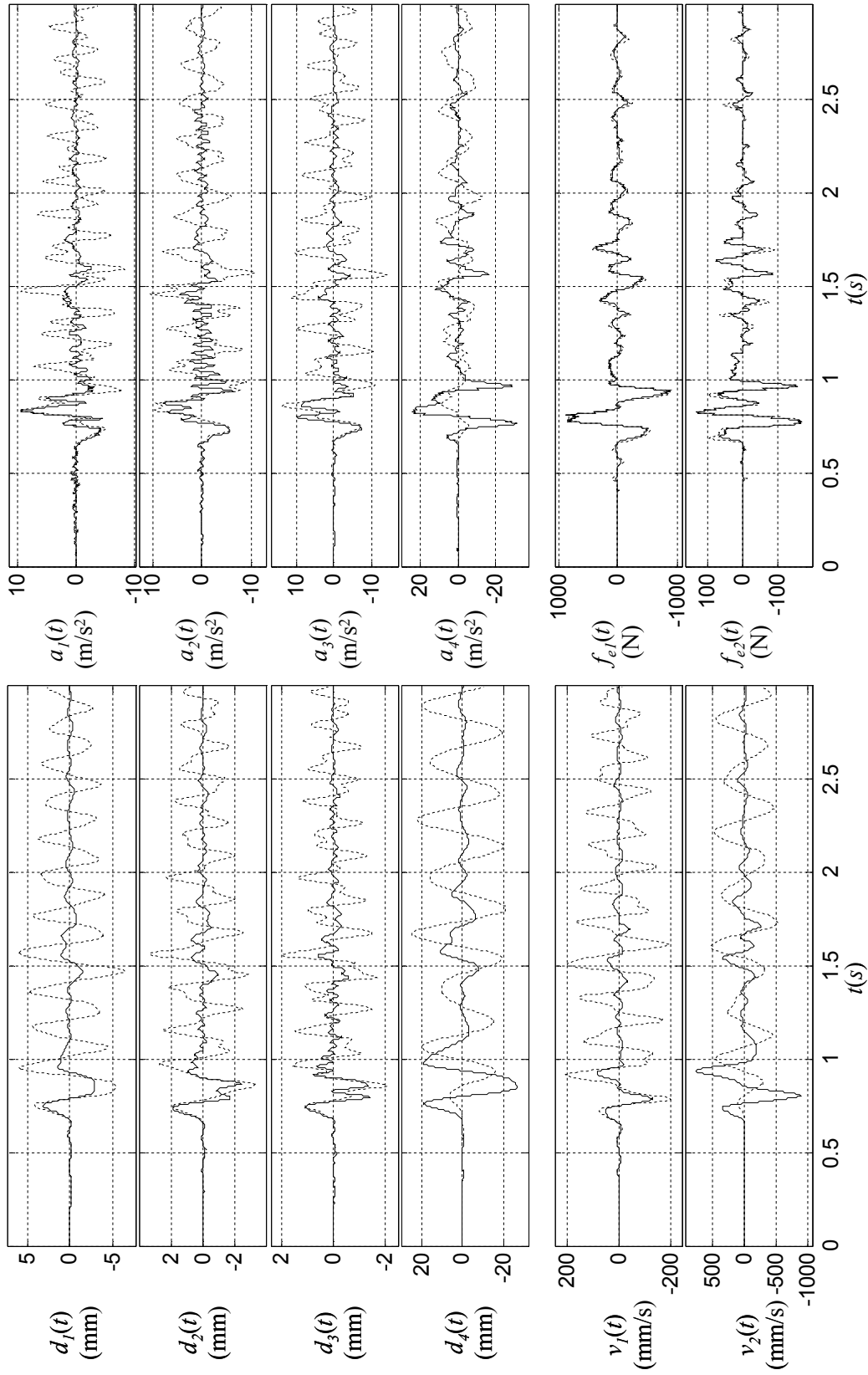


Figure 7.20a: Mechanical response quantities for Northridge earthquake with CZ control

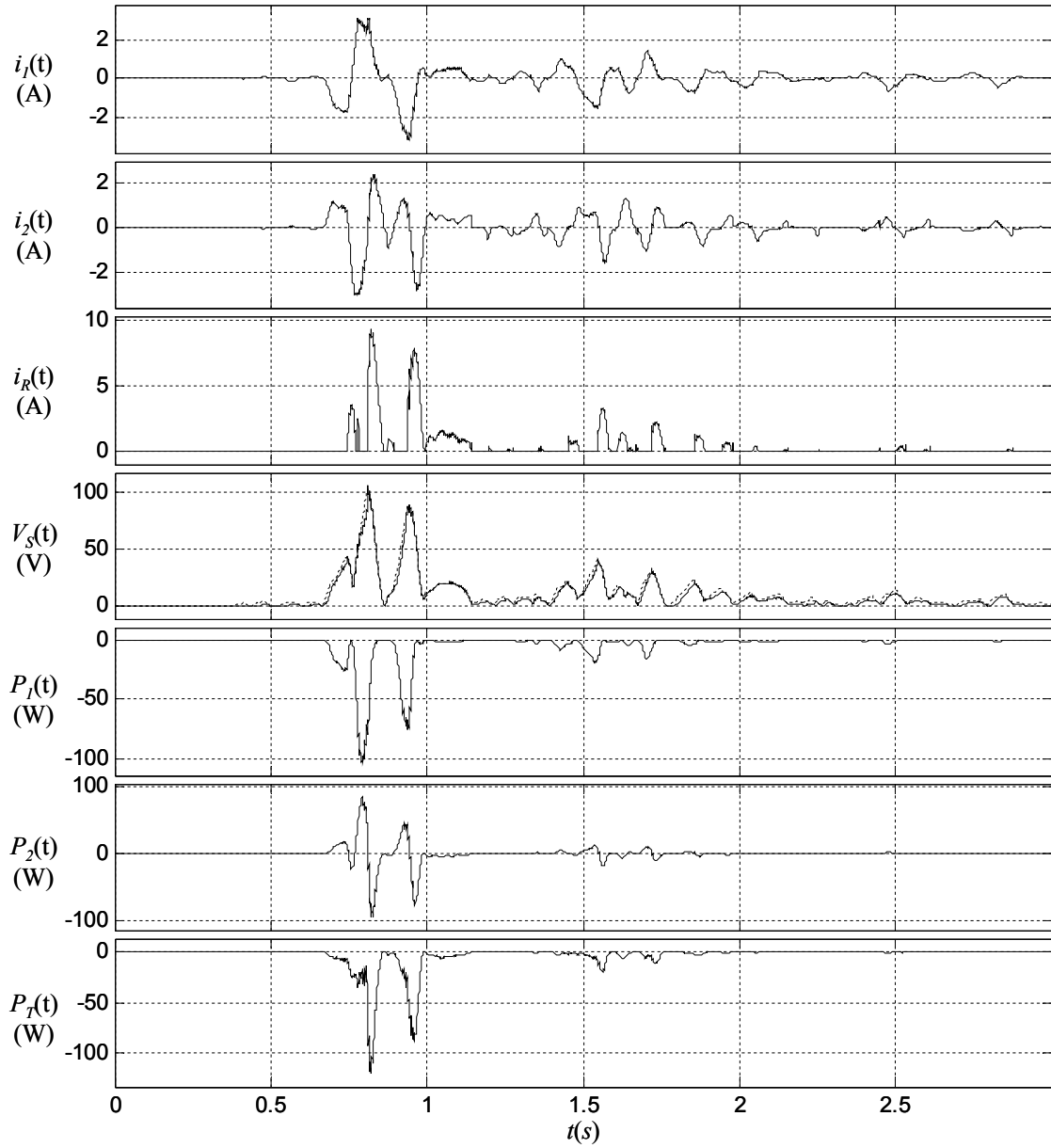


Figure 7.20b: Electrical response quantities for Northridge earthquake with CZ control